Numerical and experimental investigation for helical Savonius rotor performance improvement using novel blade shapes

Mariem Lajnef [1,*], Mabrouk Mosbahi [2,3], Hasna Abid [1], Zied Driss [1], Emanuele Amato [3,4], Calogero Picone[3], Marco Sinagra[3], Tullio Tucciarelli [3,4].

[1]Laboratory of Electro-Mechanic Systems (LASEM), National School of Engineers of Sfax (ENIS), University of Sfax, B.P. 1173, km 3.5 Soukra, 3038 Sfax, Tunisia

[2]University of Tunis, Higher National Engineering School of Tunis (ENSIT), Avenue Taha Hussein Montfleury, 1008 Tunisia

[3]University of Palermo, Department of Engineering, 90128 Palermo, Italy

[4]Sustainable Mobility Center (Centro Nazionale per la Mobilità Sostenibile-CNMS), Italy

* Corresponding author. Tel.: + 216 74 274 409; Fax: + 216 74 275 595.

E-mail address: mabrouk.mosbahi@gmail.com

Abstract

Wind energy is extensively invested as a renewable and clean energy source. Savonius wind rotor, as an energy converter, has the merit of being appropriate for specific applications. The current paper centers around the performance enhancement of a helical Savonoius wind rotor through blade shape optimization. The basic objective is to assess numerically and experimentally, in addition to the helical Savonius rotor, two novel rotor blade shapes named delta bladed and two-stage delta bladed shape. Numerical study was conducted using Ansys Fluent software. 3-D unsteady simulations were carried out through the use of the SST k-ω turbulence model based on the finite volume method solver. Aerodynamic flow and performance characteristics were investigated. Static and dynamic experimental tests were undertaken on a wind tunnel. An improvement in C_p by 22.58 % and 29.5 % for the two-stage delta bladed rotor and 19.35 % and 16.4 % for the delta bladed rotor over the helical Savonius rotor was recorded, respectively, numerically and experimentally. In addition, the self-starting ability as well as the aerodynamic flow characteristics of the helical rotor were enhanced with the novel blade shapes.

The obtained findings can be regarded as technologically significant in terms of opening further fruitful lines of investigations and promising future research direction as far as the use of helical Savonius wind turbine is concerned.

Keywords: Helical Savonius rotor, delta bladed shape, two-stage delta bladed shape, performance characteristics, aerodynamic flow characteristics.

1. Introduction

The global energy demand is growing, while the fossil fuel sources are likely to run out. As a result of the extravagant use of the conventional fossil sources, the world has also been facing environmental threats related to the emission of a huge amount of pollutants. To overcome these problems, wind energy technology as an alternative to fossil fuels, has been a hot area of research triggering significant scientific concern and whetting the interest among both scientists and industrials.

As an inexhaustible and a friendly environmental source of energy, wind energy has been considered among the most outstanding renewable energy used to meet domestic and industrial demands. Wind turbines, defined as the wind energy converter, are basically classified into two classes: (HAWT) horizontal axis wind turbines and (VAWT) vertical axis wind turbines. This classification relies notably on the alignment between the coming wind direction and the turbine rotation axis. Within the wind energy, the HAWT have been the most commonly used for electricity requirements over the recent years. Compared to the VAWT, the horizontal ones display higher power efficiency but they require permanent wind direction to be more powerful. However, the vertical axis wind turbines have inherent specifications. As they operate independently from wind direction with a lower cost of installation and maintenance and without a need for yaw mechanism, VAWT are required in specific implementations. The operating principle rests on the momentum force difference that turns into a pressure difference between the convex and concave side of the rotor blades triggering subsequently the turbine rotation around a vertical shaft. VAWT, based on the driven force, are categorized into the lift force-based Darrieus rotor and the drag force-based Savonius rotor[1]. Despite having a lower power efficiency compared to HAWT and Darrieus turbines, the Savonius rotors have significant merits. As a drag machine, it operates thanks to the drag force resulting from its blades. It is to be noted that it also adds the lift force that

77 contributes to an amount of power production. The Savonius wind turbine can further operate
78 under turbulent flow, independently from the wind direction and with a good self-starting
79 ability[2]. Additionally, it has a simple structure, a lower cost of fabrication and maintenance, a
80 lower noise emission and maintains the most stable performances. Two blades having a semi-
81 cylindrical shape mounted from either side of a vertical shaft make up its original design,
82 which creates an outlook that seems analogous to an "S" shape. This concept is meant to
83 instill the incoming wind to the turbine blades.
84 The overlap ratio, the aspect ratio, the number of stages and blades, the end plates, and the
85 blade shape stand for the main geometrical parameters influencing the conventional Savonius
86 wind turbine performance. Its efficiency can equally be affected by adding accessories.
87 Several investigations have reported both numerically and experimentally that the Savonius
88 rotor performance has been improved across parametric optimization. With regard to adding
89 accessories, the principle relies on harvesting the wind to the concave side of the advancing
90 blade and precluding the convex side of the returning blade. In this respect, numerous designs
91 were investigated. In fact, it was about deflecting plates installed upstream the rotor composed
92 of one[3], two[4,5,6] or even a set of plates[7], a whole deflector system[8,9], a curtain arrangement[10] as
93 well as a guiding box[11]. It was found that the output performances mainly the torque and the
94 power coefficients as well as the aerodynamic characteristics of the Savonius rotor were well
95 improved with the use of those accessories. Regarding the optimization of the rotor
96 geometrical parameters, the overlap ratio was examined. Numerically, Hassanzadeh et al.[12]
97 recorded inward and outward overlap ratios and deduced that 0.2 was the optimum one. Patel
98 et al.[13] investigated numerically negative overlap ratios varying from 0 to 0.4 and revealed that
99 the zero one provided the maximum power coefficient equal to 0.09 at a tip speed ratio of 0.6.
100 As far as the aspect ratio is concerned, it was inferred that its rise enhances the torque
101 coefficient, although it lowers the rotational speed since the structure becomes heavier[14].

That's why, for structural constraints, it is set near to 1.0 for most of the extant rotors[15]. Additionally, using end plates was equally regarded as a way to boost the goodness of fit of Savonius rotor. Within the same vein, Jeon et al.[16] experimented Savonius rotor with different configurations of lower and upper end plates. A progress of 36% in the power coefficient was reported. In fact, the inclusion of end plates stop the air escaping from the concave side of both blades, forcing it to flow from the concave advancing blade to the concave returning blade. It maintains a greater pressure difference between the concave and convex sides of the rotor blades along the rotor height. As a result, it minimizes the negative drug and improves the energy conversion process. Regarding the number of blades, the rotor performance drops with its increase due to an important vortex phenomenon created close to the rotor blades[17]. In the same context, Mahmoud et al.[14] found that the two-blade Savonius rotor highlighted the highest value of power and torque coefficients compared to the three and four blades rotor. However, experimentally, Wenehenubun et al.[18] compared two, three and four blades rotors. They emphasized that the four-blade and the three-blade rotors are the most efficient, respectively, at a low and high speed ratio. Referring to the number of stages, Shamsuddin et al. [19] asserted that the double-stage rotor performance exceeded the single stage. Furthermore, the maximum power coefficient recorded was 138 % higher at 5 m/s and the self starting ability reached 5m/s while it was equal to 7 m/s with the single stage rotor. As the blade represents the main part of the Savonius wind turbine having the major impact on wind-capture capability, diligent efforts have been dedicated to optimize it to obtain better efficiency. Alom et al.[20] identified four blade profile configurations, named respectively, semi-circular, Benech, modified-Bach and elliptical then subjugated them into numerical and experimental tests. The maximum power coefficient was numerically equal to 0.27, 0.29, 0.30 and 0.34, respectively. Hence, the elliptical profile displayed the highest performance. Talukdar et al.[21] focused on the elliptical form and developed a new design. They carried out

experiments in a subsonic wind tunnel and they revealed a 37% improvement over the traditional semicircular form. In the same vein, Al Absi et al.[22] explored the blade ellipcity through firstly changing the rotor overlap ratio then modifying the inner blade surface seiing from the concave part into a zigzag regular form. Based on wind tunnel tests at a wind velocity of 9m/s, the optimum modified elliptical blade form provided a power coefficient of 0.29 which proved to be higher than the classical Savonius rotor (0.26). Asadi et al.[23] putted to test, numerically, two forms of Savonius wind rotor blades: the semi circular and the Bach-type. They proved that the rotor with the Bach-type form outperformed the traditional semicircular one with a maximum betterment of 20 % in the power coefficient at a tip speed ratio equal to 1.5. On the other side, Jia et al.[24] handled the blade curve. They set forward a new-developed two-blade Savonius rotor using the cubic Bezier curve method. The optimized blade was checked and compared to the classical one. It highlighted twofold benefits. It improved the power coefficient by 6.87% on the one hand and boosted the aerodynamic performance on the other hand. In addition, sine and conical blade forms were suggested by Abdelaziz et al.[25] and then compared to the classical blade form numerically with the use of 3-D simulations. The maximum power coefficient reduced by 1.25% with the sine form and enhanced by 8.6% with the conical form. Not too far, a blade shape inspired by sandeels fish structure was proposed by Abdelghafar et al.[26] The design form was described through the blade length, its maximum camber and its location. The optimization procedure was based on evolutionary algorithms. The optimum design exhibited an important increase in the rotor output up to 9.21 % at a tip speed ratio of 0.8. Within the same vein, modifying the twist angle was adopted as a tool to examine the change of the classical form of the Savonius rotor blades into helical one with twisted blades. Lee et al.[27] tested numerically and experimentally four helical Savonius rotors with 0°, 45°, 90° and 135° twist angles. The maximum power coefficient was recorded for 45° twist and dropped by 25.5% for 90° and 135°. Saad et al.[28]

explored five twist angles from 0° to 180° in step of 45°. With an increase in twist angle, the created torque took positive values for different rotor angles. Indeed, the helical rotor yielded a smoother machine operation with an enhanced starting ability. However, above 45° (from 90° to 180°), a diminishment in its magnitude was noticed and so maximum value was discovered with 45°. Nevertheless, a closer look into the helical Savonius rotor corroborates that there is a lack of analysis related to its design parameters optimization. Owing to its geometry complexity, it has not been utterly examined even though its substantial advantages over the traditional Savonius rotor. In this context, investigations focused mainly on the twist angle optimization[27-29]. As well, few parameters were examined, namely, the overlap ratio and the end plates size ratio[28]. The findings showed that 45° twisted Savonius rotor with zero overlap ratio and a 1.1 endplates ratio, as compared to other designs, achieved the maximum output performances. In addition, the effect of multi-stage was also examined[30]. Accordingly, it enhanced the performance of the rotor in terms of power coefficient and self-starting ability and lowered the noise and the mechanical vibrations emitted along its operation. From this perspective, the originality of the current research study lies in improving the performance of a helical Savonius wind turbine through the optimizing of its blade shape as this technique showed an important improvement but it remained restricted to the conventional Savonius rotor.

The basic target was to put in test various blade shapes of helical Savonius rotor. Indeed, in addition to the helical Savonius rotor, two novel rotor blade shapes, namely the delta bladed rotor and the two-stage delta bladed rotor were investigated numerically and experimentally. The three rotors were created using the 3D printing technology. Next, wind tunnel tests were conducted in order to get the static and dynamic experimental characteristics. Computational simulations using the ANSYS 17.0 software were performed. At this stage of analysis, we would assert that the central objective of the work at hand is to explore the blade shape

177 behavior on the characteristic performance of the helical Savonius rotor both numerically and
178 experimentally.
179
180 **2. Experimental set up and methodology**
181 This section focused on the experimental approach. In fact, all needed materials were
182 mentioned. The experimental methodology was described in details and all required
183 measuring instruments were presented.
184
185 **2.1. Design and fabrication of the rotors**
186 The additive manufacturing method rests on fabricating object additively, layer by layer
187 starting with a three dimensional numerical model created through the use of a solid modeling
188 computer-aided design (CAD). Hence, it carries directly the digital presentation into a real
189 physical model. Basically, the 3D printing can reduce costs while obtaining a longer lifetime
190 compared to other manufacturing procedures. Thus, it makes the additive manufacturing
191 method extremely beneficial and encourages its incorporation in the industrial area.
192 Through conducting a numerical and experimental investigation addressing the effect of blade
193 shape, three designs of helical Savonius rotor exhibiting different blade shapes were
194 undertaken. Referring to the geometrical complexity of rotor shapes, the 3D printing proved
195 to be the most suitable as a fabrication technology. The first step consisted in designing the
196 Savonius rotors utilizing the Solidworks software, as depicted in figure 1.a. Afterwards, the
197 digital models were brought to a 3D printer through the use of a PLA (poly lactic acid)
198 filament having a diameter of 1.75 mm. Based on the geometry section, the rotors have been
199 extruded layer by layer. When all layers were handled, the rotors were manufactured and were
200 removed from the tray for required tests, as illustrated in figure 1.b. The three proposed rotors
201 portrayed in figure 1 are named, respectively, the helical Savonius rotor, the delta bladed rotor

and the two-stage delta bladed rotor. They, all, have no gap distance and a common blade portion “P” equal to P=48.5 mm. The overall geometrical parameters displayed in Table 1 and figures 1.a and 1.c are retained for the three rotors.

2.2. Wind tunnel test facility

The experimental tests were undertaken in a wind tunnel, which was designed and fabricated to establish the aerodynamic characteristics of the investigated helical rotors[31]. The wind tunnel exhibited in figure 2 is fabricated from galvanized iron sheets and Plexiglas. It mainly includes: (1) a settling chamber, (2) a diffuser, (3) a test section consisting of Plexiglas in which the turbines are placed, (4) a collector and (5) a drive section. The shape of the test section is a parallelepiped having a width of 0.4 m as well as an equal height and a length of 0.8 m, where wind velocity varies from 0 to 9 $m.s^{-1}$. The air speed was controlled by varying the frequency of the ventilation fan of the vacuum cleaner mounted in the drive section. The settling chamber was used to make the airflow straight in the test section. Under these conditions, it was entirely turbulent and became uniform with turbulence intensity under 1%. To ascertain this fact, various points in different location along the test section, have been chosen to measure the air velocity in each point with the use of a hot wire anemometer AM-4204. It was found that the air velocity value was nearly constant in the test vein. In addition, the more the points approach the test vein walls, the more the value of the velocity decreased until reaching 0. The specifications of the used anemometer are shown in Table 2.

2.3. Experimental measurements and instrumentations

The present experimental study handles three shapes of helical Savonius rotor. It relies on putting the proposed rotors amidst the test section. Two ball bearings were fixed on either side of the shaft to ensure its free rotation guidance and to support the rotors. At a selected velocity

accordingly at a selected Reynolds number, the incoming wind force generates the blade rotation and then a rotating power emerges as a result. To identify the proposed helical Savonius rotor shapes performance and to tackle the interaction between the flow and the blades, it is significant to express the performance using well-determinate non-dimensional parameters. Static and dynamic measurements were taken for a wind velocity equal to U_∞=9 $m.s^{-1}$ accordingly for Reynolds number equal to Re= 9.8×10^4.

For the static measurements, relative to the wind direction, with the use of a static digital TQ-8800 torque meter, T_s the static torque was assessed. It is measured for different angular positions lying from 0° to 360° in a step of 10°, using a gradual disk, as highlighted in figure 3. In fact, for each angular position, the rotation of the helical rotor was jammed and the corresponding static torque value was shown through the digital display. The specifications of the used static torque meter are shown in Table 3.

Then, using equation 1, the static torque coefficient was specified. This non-dimension parameter reflects the self-starting criteria of the rotor.

$$C_{Ts} = \frac{T_s}{\frac{1}{2}\rho R A U^2_\infty} \quad (1)$$

where T_s stands for the static torque (N), U_∞ indicates the incoming wind velocity ($m.s^{-1}$), ρ refers to the air density ($kg.m^{-3}$), R corresponds to the rotor radius (m), and A expresses the projected area calculated as follows:

$$A = DH \quad (2)$$

where H and D are the height of the rotor and its diameter, respectively.

For the dynamic measurements, the rotor rotational speed Ω was determined by a CA-1727 digital tachometer model. The specifications of the tachometer are shown in Table 4.

Then, the tip speed ratio λ was estimated based on the following equation.

$$\lambda = \frac{R\Omega}{U_\infty} \tag{3}$$

Gradual loads were applied to the rotor shaft to realize the braking operation. Indeed, a 1mm of diameter inelastic nylon wire was rolled up on the shaft maintained on the one end and on the other end a load was suspended. For each load, the dynamic torque T was measured with a torque meter sensor. Its instantaneous variation was displayed across computer acquisition with the use of the installed EMPERIOR LITE software. Then the average value was recorded and associated with the corresponding measured rotational speed (subsequently a tip speed ratio). The used facilities are outlined in figure 4 and all required dynamic torque specifications are shown in Table 5.

The experimental performances of the studied helical rotors are expressed in terms of non-dimensional coefficients: the power coefficient (C_p) and the torque coefficient (C_T) as a function of the tip speed ratio (λ).

The torque coefficient C_T defined as the ratio between the effective produced and the available torque can be computed in terms of:

$$C_T = \frac{T}{\frac{1}{2}\rho R A U^2_\infty} \tag{4}$$

The power coefficient C_p corresponds to the ratio between (P_r) the rotor mechanical power and (P_w) the wind power.

$$C_p = \frac{P_r}{P_w} \tag{5}$$

The wind power is indicated as:

$$P_w = \frac{1}{2}\rho A U^3_\infty \tag{6}$$

Equation (7) indicates the mechanical power (P_r):

$$P_r = T\Omega \quad (7)$$

Hence, Cp, C_T and λ are governed by equation (8)

$$C_p = C_T \lambda \quad (8)$$

3. Numerical methodology

The Computational Fluid dynamics (CFD) have been applied to settle flow problems for multiple applications. In aerodynamics, the wind flow around turbines can be well predicted, analyzed and interpreted through solving the governing equations describing the flow phenomena. For this reason, various codes and softwares have been used (SOLIDWORKS, COSMOS-FLOWORKS, ADINA, FLOW SIMULATIONS and ANSYS). The solving procedure uses basically three primordial elements: (i) the preprocessor which consists in defining the overall domain, the generation of the mesh and the boundary conditions (ii) the solver that handles the choice of discretization method and (iii) the post processor which consists in outputting results.

As far as this research work is concerned, the numerical simulations for the proposed rotor shapes were carried out deploying ANSYS Fluent 17.0 software. It was applied to calculate the flow characteristics around complicated structures. In fact, it uses the Finite Volume Method (FVM) to resolve the Navier Stokes equations. This method is well-suited for the problem interaction between the rotating blades of the turbine and the inlet wind flow.

3.1. Simulation domain and setting of boundary conditions

The overall domain and boundary conditions considered in this work are summarized in figure 5. For suitable analysis, the overall domain was split into two sub-domains which are separated using an interface created at the level of the adjacent faces. The first surrounding domain, representing the test section, is considered as steady. The second cylindrical domain,

containing the rotor, is considered as a rotating domain with a 185 mm of diameter with an angular velocity defined with regard to the tip speed ratio. Both domains were modelized in the ANSYS design modeler. To undergo the same circumstances as those with the wind tunnel, the inlet boundary condition was set as a uniform velocity in terms of U_∞= 9 $m.s^{-1}$. The outlet was set to be an atmospheric pressure. A no-slip moving walls condition was imposed in the rotor blades with a rotational speed that is conform to the tip speed ratio. Turbulence viscosity and intensity were set respectively equal to 10% and 5% for both outlet and inlet. Inded, those values go in good consisty with those reported in the literature review[32,33] and are relative to the characteristics of the wind tunnel invested in the experiments.

3.2. Grid generation

In figure 6, the grid form of the rotor and the outer local rotating domain are illustrated. In fact, the 3D overall domain which was imported to the ANSYS meshing user interface, was discretized with the use of unstructured tetrahedral grids. Several body sizings, faces and edges were used to create finer mesh in the rotating domain compared to the steady domain.

To boost the mesh quality and to trace the boundary layers built up close to the blades of the rotor, inflation was created. Hence, a prismatic layer was generated at the boundary layer and particularly near the rotor blades. So that the created mesh is suitable, the distance (y_n) defined as the first mesh node distance from the rotor walls should be well chosen. To do that, y^+ is the appropriate parameter to set based on equation 9. The determination of the exact value of y^+ is based on the turbulence model walls law. As the SST k-w was the used one, a y^+ nearly equal to 1 was associated[34]. Twenty prismatic layers with 1.2 growth rate were created.

$$y+=\frac{\rho u_t y_n}{\mu} \tag{9}$$

where μ stands for the fluid dynamic viscosity (Pa.s) and u_t presents the friction velocity (m.s^{-1}).

A grid sensitivity test was performed to select the mesh that yields the suitable results.

3.3. Turbulence modeling and solver setting

The flow surrounding the helical Savonius rotors is naturally turbulent. For these criteria, transient simulations were undertaken. The time step, calculated as follows, should be wisely and precisely chosen.

$$\Delta t = \frac{\Delta\theta}{\Omega} \tag{10}$$

where θ indicates the rotor shaft angular position (rad). It is, in fact, the degree whereby the rotating domain, subsequently the rotor, rotates per time step. Ω denotes the rotor rotational speed (rad s^{-1}). .

A time step independency test was performed by putting in test four time steps varying from 0.5°/step to 3°/step. The opted one in this study corresponds to 1° rotation of the helical rotor. 50 numbers of iterations were taken per time step so that the wind flow would be readjusted and renewed until being stabilized. Calculations were undertaken for six complete rotor revolutions. The consistent state of the flow was obtained after four revolutions. The details were, therefore, saved from the fourth cycle. To reach the convergence, the values of the obtained results for each iteration need to be closer to the previous one. In fact, relaxation factors are fundamental to amortize the solution from the previous one so that the stability would be reached. Thus, the momentum, turbulence and continuity residuals were settled equal to 10^{-5} so as to monitor the convergence.

The resolution of the fluid dynamics problems relies on the Reynolds-Averaged Navier-Stokes equations[35,36]. Finite Volume Method was adopted to discretize them. The convective

terms as well as the temporal ones were discretized using the Second order Up-wind scheme. The SIMPLE scheme (Semi-Implicit Methods for Pressure-Linked Equation) was applied to infer the relation between the pressure and the velocity in the overall domain. The Navier-Stokes governing equations according to a Newtonian fluid are prescribed under the continuity equation indicated in (11) and the momentum equation indicated in (12).

$$\frac{\partial \rho}{\partial t} + \frac{\partial (\rho u_i)}{\partial x_i} = 0 \tag{11}$$

where t corresponds to the time (s) and u_i expresses the velocity component defined in the x_i coordinate direction x_i=(x,y,z).

$$\frac{\partial (\rho u_i)}{\partial t} + \frac{\partial (\rho u_i u_j)}{\partial x_j} = -\frac{\partial p}{\partial x_i} + \frac{\partial}{\partial x_j}\left[\mu\left(\frac{\partial u_j}{\partial x_j} + \frac{\partial u_j}{\partial x_i} - \frac{2}{3}\delta_{ij}\frac{\partial u_i}{\partial x_i}\right)\right] + \frac{\partial\left(-\rho\overline{u_i' u_j'}\right)}{\partial x_j} + F_i \tag{12}$$

where F_i indicates the external forces applied (N) and p denotes the pressure (Pa).

The components of the Reynolds stress tensor are determined mathematically through equation (12).

$$-\rho\overline{u_i' u_j'} = \mu_t\left(\frac{\partial u_i}{\partial x_j} + \frac{\partial u_j}{\partial x_i}\right) - \frac{2}{3}\rho k \delta_{ij} \tag{13}$$

where x_i, x_j corresponds to the Cartesian coordinate, μ_t refers to the turbulent viscosity (Pa.s), δ_{ij} stands for the Chronecker indices and k expresses the turbulent kinetic energy (Pa.s).

Four turbulence models, namely, the Standard k-ε, the RNG k-ε, the Realizable k-ε and the SST k-ω were put to test under this study to clarify their effects on the numerical results. The Shear Stress Transport (SST) k-ω model was adopted for the current simulations. Many researchers demonstrated previously its good capability to modelize the wind turbines as well as its good ability to predict the flow patterns[37,39]. In fact, the SST k-ω model combines the k-ω model accuracy and robustness in the near wall regions and the k-ε model free flow in the

far wall regions. In this line, Nasef et al.[40] tested the four turbulence models and proved that the SST k-ω model yielded optimal results.

The turbulence kinetic energy (k) is expressed in terms of:

$$\frac{\partial(\rho k)}{\partial t}+\frac{\partial(\rho u_i k)}{\partial x_i}=\frac{\partial}{\partial x_i}\left[\left(\mu+\frac{\mu_t}{\sigma_k}\right)\mathrm{grad}(k)\right]+2\mu_t\frac{\partial u_i}{\partial x_j}\cdot\frac{\partial u_i}{\partial x_j}-\frac{2}{3}\rho k\frac{\partial u_i}{\partial x_j}\delta_{ijk}-\beta^*\rho k\omega \tag{14}$$

The specific dissipation rate (ω) is indicated by:

$$\frac{\partial\rho\omega}{\partial t}+\frac{\partial(\rho u_i\omega)}{\partial x_i}= \\ \frac{\partial}{\partial x_i}\left[\left(\mu+\frac{\mu_t}{\sigma_{\omega,1}}\right)\mathrm{grad}(\omega)\right]+\gamma_2\left(2\rho\frac{\partial u_i}{\partial x_j}\cdot\frac{\partial u_i}{\partial x_j}-\frac{2}{3}\rho\omega\frac{\partial u_i}{\partial x_j}\delta_{ij}\right)-\beta_2\rho\omega^2+2\frac{\rho}{\sigma_{\omega,2}\omega}\frac{\partial k}{\partial x_k}\frac{\partial\omega}{\partial x_k} \tag{15}$$

where β^*, β_2, σ_k, $\sigma_{\omega,1}$, $\sigma_{\omega,2}$ and γ_2 indicate the constants of the SST k-ω turbulence model and μ expresses the dynamic viscosity (Pa.s).

4. Results and discussion

4.1. Experimental results

The rotors with the proposed shapes were put to test to control the static torque coefficient (C_{Ts}), the power coefficient (C_p) and the torque coefficient (C_T). The static torque is often used to describe the starting feature of the Savonius wind turbine. Figure 7 illustrates the C_{Ts} versus the azimuths for the tested blade shapes. It is quite obvious that the variation of the static torque coefficient is periodic with a 180° cycle. The static torque coefficient increases progressively until achieving its peak. The highest C_{Ts} holds the value of 0.161, 0.178 and 0.184 for an azimuth of 100°, 70° and 60° for the helical, the delta bladed and the two-stage delta bladed rotors, respectively. Concerning the remaining cycle, the static torque coefficient drops to reach its minimum at 180°. Regarding these observations, the maximum value of the static torque coefficient is determined from a maximum quantity of the air that has attacked

the concave side of the blade for the corresponding angular position. Yet, its minimum value is specified from the air force that has not suitably moved to the concave side of the blade at the matching azimuth. Hence, the graph indicates that the two-stage delta bladed rotor displays an improvement with regard to the starting performance over the delta bladed and the helical Savonius rotors.

Referring to the tip speed ratio in a range varying from 0.4 to 1.2, (C_T), the torque coefficient and (C_p) the power coefficient were computed before being plotted in figures 8.a and 8.b, respectively. Departing from figure 8.a, it is inferred that the torque coefficient is inversely proportional to the tip speed ratio. This fact is related to the application of gradual loads which not only minimizes the rotational speed of the turbine but also increases the value of the rotor torque. The highest value of the torque coefficient is obtained at a tip speed ratio around λ=0.44. It seems to be equal to 0.214, 0.224 and 0.251 for the helical Savonius rotor, the delta bladed rotor and the two-stage delta bladed rotor, respectively. Relying upon figure 8.b, the power coefficient increments with the augmentation in the tip speed ratio until reaching its peak over which it decays even with the augmentation in the tip speed ratio. The peaks of the power coefficient value proved to be 0.122, 0.142 and 0.158 at a tip speed ratio of 0.7, 0.78 and 0.86 for the helical Savonius rotor, the delta bladed rotor and the two-stage delta bladed rotor. Therefore, the two-stage delta bladed rotor revealed experimentally an enhancement of C_p, C_T and even C_{Ts}. Interestingly, an improvement in C_p by 29.5 % for the two-stage delta bladed rotor and 16.4 % for the delta bladed rotor over the helical Savonius rotor was recorded departing from experimental tests. It is noteworthy that both proposed novel shapes displayed a better interaction between the projected area of the rotor blades and the incoming flow. Hence, a higher C_p was obtained over the helical Savonius rotor.

Table 6 exhibits the experimental uncertainties on λ, C_{Ts}, C_p and C_T for the suggested rotors at a Reynolds number equal to Re= 9.8×10^4. Table 7 displays the experimental error for the different used measurement instruments in this study.

4.2. Numerical model validation

A grid study was performed for the generated mesh to offer well estimated numerical results with respect to the corresponding experiments. Indeed, a mesh refinement was undertaken wherein the size of the generated mesh progressively increased until the computational results didn't undergo a significant alteration. The simulations were carried out for the helical Savonius rotor with four grid sizes, named coarse, medium, fine and extra fine having 260000, 570000, 880000 and 1.3 million nodes, respectively. At a tip speed ratio λ=0.73 and for the proposed mesh sizes, the torque coefficient versus the azimuth is plotted in figure 9. A good agreement was detected between the extra fine and the fine mesh. However, the error was more important for the coarse and the medium grid. At this stage, the fine grid could be chosen for the following simulations considering numerical precision and time saving.

Furthermore, the turbulence model effect was investigated. Four turbulence models, namely, the SST k-ω, the RNG k-ε the standard k-ε and the realizable k-ε were examined. Figure 10 depicts the effect of the turbulence model on the torque coefficient of the helical Savonius rotor at λ=0.73. A good agreement between the SST k-ω and the realizable k-ε was recorded in comparison with experimental data. However, the RNG k-ε and the standard k-ε are far away from them. Resting upon these and since the SST k-ω was regarded as an appropriate model for many researchers as clarified above, it was adopted for the following simulations.

Moreover, the time step independency test was performed by putting in test four time steps varying from 0.5°/step to 3°/step. Figure 11 illustrates the effect of the time step on the torque coefficient of the helical Savonius rotor at λ=0.73 in a steady phase. It is clear that with higher

degree per step exactly 3°/step and 2°/step, the average value of the torque coefficient decreases. This is because the flow mechanics, close to the rotor blades, are not effectively captured. This fact increases the error between numerical and experimental findings. Considering that the two time steps 1°/step and 0.5°/step gave approximately similar torque coefficient variation, the 1°/step time was selected under this study to save time calculation.

We enacted a comparison between experimental and numerical results in order to assess the goodness of fit and reliability of the CFD model. Figure 12 depicts both experimental and numerical power coefficients of the helical Savonius rotor. The average error is about 5% for a tip speed ratio ranging from 0.4 to 1.2. From this perspective, it is noteworthy that the simulation findings go in good conformity with the experimental ones. For this reason, we may assert that the CFD model is suitable to assess the effect of the proposed blade shapes on the efficiency of the helical Savonius wind rotor.

4.3. Numerical results

4.3.1 Aerodynamic flow characteristics

Magnitude Velocity

Figure 13 illustrates the velocity distributions for the two-stage delta bladed, the delta bladed and the helical rotors at a tip speed ratio λ=0.73. The velocity upstream the rotor seems to be uniform and takes the value of V=9 $m.s^{-1}$, as put in the entry boundary conditions. A deceleration near the rotor blades turns out to be in the range of 4-5 $m.s^{-1}$ for the suggested shapes. The vortices formation in the concave side of the returning blades is more considerable for the two-stage delta bladed rotor. At this stage, the flow passage is more significant which lessens the negative drag and enhances the turbine rotation anti-clockwise. The maximum velocity region is situated on the convex side of the returning blade (figure 13.a). It proves to be lower in the two-stage delta bladed rotor than the others. It is equal to

V=14.6 m.s^{-1}, V=15.3 m.s^{-1} and V=16.7 m.s^{-1}, respectively, for the two-stage delta bladed, the delta bladed and the helical Savonius rotor. Indeed, it indicates a less important negative drag and, as a matter of fact, a higher power coefficient Cp compared to the others. A wake zone of velocity, downstream the rotor, is clearly detected. In figure 13.b, the wake shape is lucid and influenced by the rotor blade shape. The wake formation refers basically to the centrifugal force that is responsible for the blades rotation. Moreover, a symmetrical aspect is depicted for all configurations, but proves to be more significant for the two-stage delta bladed rotor.

With regard to the same axial position z=0.097 m and for a y direction lying from y=-0.27 m to y=0.27 m, various points are produced for each transversal plane identified respectively by x=-0.3 m, x=-0.08 m, x=0.08 m and x=0.3 m. The velocity profiles for those specific points and for all the examined rotor shapes are plotted in figure 14. The velocity evolution upstream and downstream the rotor reinforces what was mentioned before. In fact, at upstream x=-0.3 m (figure 14.a), the velocity holds the value of the inlet condition V=9 m.s^{-1}. A sharply deceleration is detected in figure 14.b which stands for the area near the rotors. Figures 14.c and 14.d reveal a drop in the velocity downstream. This drop introduces the wake zone. It becomes more significant while moving away from the rotor and proves to be more notable for the two-stage delta bladed rotor (figure 14.d). Indeed, it is clearly inferred that the two-stage delta bladed rotor is more efficient than other rotor shapes.

Total pressure

The total pressure distributions for the two-stage delta bladed, the delta bladed and the helical Savonius rotor at a tip speed ratio λ=0.73 are highlighted in figure 15 at a tip speed ratio λ=0.73. The pressure distribution for all proposed configurations exhibits two basic characteristic features: a high and a low-pressure zone. In fact, the high pressure zone manifests upstream the rotor. With a uniform aspect, it holds almost the same value for all the

rotor shapes (around 65 Pa). As for the low pressure zone, it appears around the rotor and more clearly downstream the advanced blade. By zooming on the rotating area, one can notice that the distribution of the total pressure on both the advanced and the returning blade is completely different for the proposed shapes. The pressure difference is responsible for the turbine anti-clockwise rotation. In fact, the higher total pressure value on the convex side of the returning blade is obtained for the helical Savonius rotor (p=72.56 Pa). It is relatively less significant for the two-stage delta bladed rotor (p=70.73 Pa) and the delta bladed rotor (p=68.45 Pa). Hence, the negative drag decreases with the novel blade shapes. As for the advancing blade concave side, the total pressure is more significant for the two-stage delta bladed rotor (p=-3.2 Pa) than for the delta bladed rotor (p=-5.9 Pa) as well as the helical Savonius rotor (p=-11.85 Pa) even in negative values. At this level, the positive drag is improved with the novel two-stage delta bladed shape. This, therefore, results in a higher torque for the two-stage delta bladed Savonius rotor. Additionally, it is obvious departing from figure 15.b that there is a significant change in the total pressure behind the rotors. It is related in fact to the vortices formation which is more significant for the two-stage delta bladed rotor over the others. The blade shape promotes in a straight forward way the pressure recovery. Indeed, here the wake phenomenon is clear again. Consequently, the drag force would be more significant for the two-stage delta bladed Savonius rotor. Hence, the novel two-stage delta bladed shape performance proves to be optimal compared to the other blade shapes.

To gain a better and deeper insight into the pressure comparison in different rotor positions, the pressure coefficient distribution upon the concave side of the advancing blade and on the convex side of the returning blade is outlined in figures 16 and 17, respectively, during one revolution for the proposed rotor shapes at λ=0.73. Following the power coefficient (C_{pr}) evolution versus the angular position (Θ), it is worth noting that the C_{pr} drops with the rise of

Θ in the range of (0-180°). Notably, with the turbine rotation, the blade projected area varies compared to the incoming wind direction. As a matter of fact, the topmost value of C_{pr} is obtained for Θ=0° for all configurations and for both concave and convex side (maximum projected area). With respect to the maximum pressure coefficient on the concave side of the advanced blade (figure 16), the two-stage delta bladed rotor displays a higher value of (C_{pr} =0.53) than the delta bladed (C_{pr}=0.36) and the helical Savonius rotor (C_{pr}=0.21). With respect to the maximum value of the power coefficient on the returning blade convex side (figure 17), the two-stage delta bladed exhibits equally a better value of (C_{pr}=1.94) compared to the delta bladed (C_{pr}=1.84) as well as the helical Savonius rotor (C_{pr}=1.74). Moreover, the lower value of C_{pr} is recorded for Θ=120° (lower projected area). Furthermore, the two-stage delta bladed rotor indicates the optimum values in this angular position on both concave side of the advanced blade (C_{pr}=-1.09) and the convex side of the returning blade (C_{pr}=-2.85). At this stage of synthesis, it is clearly inferred that the novel two-stage delta bladed rotor stands for the optimal shape regarding the pressure coefficient for almost all angular positions.

The turbulent intensity

Figure 18 illustrates the turbulent intensity distribution for the introduced rotor shapes at a tip speed ratio amounting to λ=0.73. Upstream, the turbulent intensity seems to be weak for all the configurations. Near from the rotating domain and more precisely behind the returning blade concave side, the turbulent intensity for the two-stage delta bladed rotor is lower lying within the range of 0.051-0.115. Nevertheless, it lies in the range of 0.067-0.121 and 0.073-0.146, respectively, for the delta bladed and the helical Savonius rotor, which collaborates a better flow passage to the concave returning blade. Downstream, the turbulent intensity is more pronounced. The symmetrical aspect is more observed for the novel two-stage delta bladed rotor than for others (figure 18.b). However, for the helical Savonius rotor the

519 maximum value is close to 0.2. The value of 0.189 and 0.179 recorded for the delta bladed
520 and the two-stage delta bladed rotor, respectively, are indicative of the wake flow zone as
521 stated before. Consequently, the turbulent intensity is less important in the case of the two-
522 stage delta bladed rotor. A lower value of the turbulent intensity involves less fluctuations
523 suggesting, therefore, a better performance in terms of flow passage and, hence, a better
524 rotation anti-clockwise.
525
526 **4.3.2 Performance characteristics**
527 The variation of the torque coefficient versus the angular position Θ for one revolution is
528 foreground in figure 19 for the examined rotor blade shapes at λ=0.73. Departing from these
529 results, it is deduced that the modification of the blade shape influences positively the
530 variation of the torque coefficient of the helical Savonius wind rotor. Indeed, its average value
531 moves from C_T=0.17 for the helical Savonius rotor to C_T=0.19 and C_T=0.2 for the delta
532 bladed and the two-stage delta bladed rotor, respectively. Accordingly, a significant
533 enhancement at the level of the predicted produced torque is recorded which is justified by the
534 enhancement of the positive drug applied on the advancing blade on the one hand and the
535 reduction in terms of the negative drug applied on the returning blade on the other hand,
536 resulting in an improved net torque thanks to the novel blade shapes.
537 The effect of the blade shape on the helical Savonius wind rotor efficiency was assessed. A
538 superposition of the experimental as well as the numerical power coefficients for a wide
539 variety of tip speed ratios ranging from λ=0.4 to λ=1.2 is highlighted in figure 20 for the two-
540 stage delta bladed, the delta bladed and the helical rotors. Relying upon the numerical results,
541 the maximum power coefficients prove to equal $C_{p,max}$= 0.124, $C_{p,max}$= 0.148 and $C_{p,max}$=
542 0.152 at a tip speed ratio of λ= 0.73, λ= 0.8 and λ= 0.88 respectively for the helical Savonius
543 rotor, the delta bladed rotor and the two-stage delta bladed rotor. Thus, numerically an

improvement in C_p by 22.58 % for the two-stage delta bladed rotor and 19.35 % for the delta bladed rotor over the helical Savonius rotor is reported.

In the same vein, a remarkable enhancement in terms of the power coefficient is obtained experimentally and validated numerically with the novel blade shapes. The two-stage delta bladed rotor displays the highest efficiency over the other rotors. A better interaction between the projected area of the rotor blades and the incoming flow with a better starting capability yielding therefore a higher C_p are reported over the helical Savonius rotor.

4.3.3. Comparison with previous studies

The current study results comprising of the blade shape impact on the helical Savonius wind rotor are compared to results accessible in the literature. Table 8 gives all necessary details. The comparison denotes that, the proposed researches were realized under similar wind speed conditions and with neighboring rotors geometric parameters mainly an aspect ratio near to 1 and 0 overlap distances. The present study highlights important and well-ranked value of power coefficients compared with others. It shows a $C_{p\ max}$= 0.152 with the optimum blade shape design which is slightly lower than some works and rather higher than other.

5. Conclusions

In the present study, in view of performance betterment of a helical Savonius wind turbine, the blade shape optimization was explored both experimentally and numerically. For this, two-novel blade shape rotors, named delta bladed and two-stage delta bladed in addition to a helical Savonius rotor were investigated. Experimental tests were conducted in a wind tunnel for a Reynolds number equal to Re= 9.8×10^4. Numerical tests were conducted using Ansys Fluent software through 3-D unsteady simulations. The main conclusions obtained under this study are:

- Departing from the wind tunnel tests, a considerable improvement in C_p by 29.5 % for the two-stage delta bladed rotor and 16.4 % for the delta bladed rotor over the helical Savonius rotor was recorded.
- The torque coefficient was equally enhanced. At λ=0.44, highest value reached $C_{T,max}$=0.251 and $C_{T,max}$=0.224 for the two-stage delta bladed and the delta bladed rotor, respectively, while it was equal to $C_{T,max}$=0.214 for the helical Savonius rotor.
- The starting ability was evenly boosted as a significant amelioration in the static torque coefficient. The highest C_{Ts} holds the value of $C_{Ts,max}$= 0.184 and $C_{Ts,max}$= 0.178 for the two-stage delta bladed and the delta bladed rotor, respectively, over the helical rotor $C_{Ts,max}$= 0.161.
- Numerically, the aerodynamic flow characteristics were improved with the novel blade shapes as a considerable betterment in the flow velocity and the pressure recovery were observed mainly around the rotor blades.
- The maximum power coefficient was higher by 22.58 % for the two-stage delta bladed rotor and 19.35 % for the delta bladed rotor over the helical Savonius rotor. It reached $C_{p,max}$= 0.152 for the two-stage delta bladed rotor, $C_{p,max}$= 0.148 for the delta bladed rotor until it was equal to $C_{p,max}$= 0.124 for the helical rotor at a tip speed ratio of λ= 0.88, λ= 0.8 and λ= 0.73respectively.
- At λ=0.73, the torque coefficient of the helical Savonius wind rotor was positively influenced with the modification of its blade shape. Indeed, its average value moved from C_T=0.17 for the helical Savonius rotor to C_T=0.19 and C_T=0.2 for the delta bladed and the two-stage delta bladed rotor, respectively.

Resting on the obtained results, the novel two stage delta bladed rotor shape, exhibited an important improvement in the aerodynamic performance over the delta bladed and the helical

Savonius rotor. Its use will therefore bring such a positive impact that it may revolutionize technological as well as industrial applications.

As a final note, we would assert that this synthesis can be regarded as promising as it may constitute a powerful impetus for researchers to explore further this area. During the research phase, it is discovered that there is still much opportunity for improvement. In future work, we plan to improve the performance of the studied helical Savonius rotor using deflector system.

Acknowledgement

The authors are thankful to the Laboratory of Electro Mechanic Systems (LASEM) members for the valuable financial assistance.

Nomenclature

A Projected area, m^2

A_r Aspect ratio, dimensionless

C_{Ts} Coefficient of the rotor static torque, dimensionless

$C_{Ts,max}$ Maximum coefficient of the rotor static torque, dimensionless

C_p Coefficient of the rotor power, dimensionless

$C_{p,max}$ Maximum coefficient of the rotor power, dimensionless

C_T Coefficient of the rotor torque, dimensionless

$C_{T,max}$ Maximum coefficient of the rotor torque, dimensionless

C_{pr} Coefficient of the rotor blade surface pressure, dimensionless

D Rotor diameter, m

D_e End plate diameter, m

d Blade chord length, m

618 e Overlap distance, m

619 F_i External applied forces, N

620 G_k Production term of turbulence, $kg.m^{-1}.s^{-3}$

621 H Rotor height, m

622 k Turbulent kinetic energy,$m^2.s^{-2}$

623 p Pressure, Pa

624 P_r Mechanical power, W

625 P_w Power of the wind, W

626 R Rotor radius, m

627 R_e Reynolds Number, dimensionless

628 s Rotor shaft diameter, m

629 t Time, s

630 T Dynamic torque, N.m

631 T_s Static torque, N.m

632 u_i Velocity component specified in the x_i coordinate direction, $m.s^{-1}$

633 $u_i^{'}$ Fluctuating velocity components, $m.s^{-1}$

634 $\overline{u_i^{'}u_j^{'}}$ Components of the Reynolds stress tensor, $m^2.s^{-2}$

635 U_∞ Velocity Incoming wind, ms^{-1}

636 V Velocity of the flow around the rotor, ms^{-1}

637 x Cartesian coordinate, m

638 x_i Cartesian coordinate, m

639 y Cartesian coordinate, m

640 y^+ Non dimensional parameter

641 z Cartesian coordinate, m

642 β^* Constant of k-ω turbulent model

643 β_2 Constant of k-ω turbulent model

644 σ_k Constant of k-ω turbulent model

645 $\sigma_{\omega,1}$ Constant of k-ω turbulent model

646 $\sigma_{\omega,2}$ Constant of k-ω turbulent model

647 θ Rotor shaft angular position, rad

648 μ Dynamic viscosity (Pa.s)

649 μ_t Turbulent viscosity, Pa.s

650 ρ Air density, $kg.m^{-3}$

651 Ω Rotor rotational speed, $rad.s^{-1}$

652 λ Tip sped ratio, dimensionless

653 ψ Twist angle ,°

654 δ_{ij} Chronecker indices

655 γ_2 Constant of k-ω turbulent model

656 Δt Time step, s

657

658 **References**

659 [1] Shende V, Patidar H, Baredar P. et al. A review on comparative study of Savonius wind
660 turbine rotor performance parameters. Environ Sci Pollut 2022; 29:69176–69196.
661 https://doi.org/10.1007/s11356-022-22399-w

662 [2] Zhou T, Rempfer D. Numerical study of detailed flow field and performance of Savonius
663 wind turbines. Renewable Energy 2013;51:373-81.

664 [3] Putri N.P, Yuwono T, Rustam J et al. Experimental studies on the effect of obstacle
665 upstream of a Savonius wind turbine. SN Appl. Sci. 2019; 1: 1216.
666 https://doi.org/10.1007/s42452-019-1253-2

667 [4] Mohamed M.H, Alqurashi F, Thévenin D. Performance enhancement of a Savonius
668 turbine under effect of frontal guiding plates. Energy Reports 2021;7: 6069-6076. ISSN 2352-
669 4847.https://doi.org/10.1016/j.egyr.2021.09.021.
670 [5] Saikot M.M.H, Rahman M, Hosen M.A. et al. Savonius Wind Turbine Performance
671 Comparison with One and Two Porous Deflectors: A CFD Study. Flow Turbulence
672 Combust 2023.
673 https://doi.org/10.1007/s10494-023-00459-6
674 [6] Salleh M.B, Kamaruddin N.M, Mohamed-Kassim Z, The effects of deflector longitudinal
675 position and height on the power performance of a conventional Savonius turbine, Energy
676 Conversion and Management 2020; 226:113584.
677 ISSN 0196-8904, https://doi.org/10.1016/j.enconman.2020.113584.
678 [7] Storti B.A, Dorella J.J, Roman N.D, Peralta I, Albanesi A.E. Improving the efficiency of a
679 Savonius wind turbine by designing a set of deflector plates with a metamodel-based
680 optimization approach. Energy 2019;186:115814. ISSN 0360-5442,
681 https://doi.org/10.1016/j.energy.2019.07.144.
682 [8] Idrissi M.S, Selmi N.& Chrigui M. Efficiency improvement of Savonius wind turbine by
683 mean of novel deflector system. J Braz. Soc. Mech. Sci Eng 2023; **45**: 396.
684 https://doi.org/10.1007/s40430-023-04330-7
685 [9]Layeghmand K, Ghiasi Tabari N & Zarkesh M. Improving efficiency of Savonius wind
686 turbine by means of an airfoil-shaped deflector. J Braz. Soc. Mech Sci. Eng 2020; **42**: 528.
687 https://doi.org/10.1007/s40430-020-02598-77.
688 [10] Altan B.D, Atılgan M, Aydog˘anOzdamar. An experimental study on improvement of a
689 Savonius rotor performance with curtaining. Experimental Thermal and Fluid Science
690 2008;32:1673-1678.

691 [11] Irabu K, Roy J.N. Characteristics of wind power on Savonius rotor using a guide-box
692 tunnel. Experimental Thermal and Fluid Science 2007;32:580-586.
693 [12] Hassanzadeh R and Mohammad Nejad.M. Effects of inward and outward overlap ratios
694 on the two-blade Savonius type of vertical axis wind turbine performance. International
695 Journal of Green Energy 2019;16:1485-1496.
696 [13] Patel J.S., Patel V.K, Rathod V.P. Influence of Negative Overlap Ratio on the
697 Performance of Semicircular Savonius Rotor with Straight Edge Extension on Overlap
698 Region. In: Doolla, S., Rather, Z.H., Ramadesigan, V. (eds) Advances in Clean Energy and
699 Sustainability 2023. ICAER 2022. Green Energy and Technology. Springer, Singapore.
700 https://doi.org/10.1007/978-981-99-2279-6_27
701 [14] Mahmoud N.H, El-Haroun A.A, Wahba E, Nasef M.H. An experimental study on
702 improvement of Savonius rotor performance. Alexandria Engineering Journal 2012;51:19-25.
703 [15] Payambarpour S.A, Najafi A.F, Magagnato F. Investigation of deflector geometry and
704 turbine aspect ratio effect on 3D modified in-pipe hydro Savonius turbine: Parametric study.
705 Renewable Energy 2020 ; 148 : 44-59. ISSN 0960-1481,
706 https://doi.org/10.1016/j.renene.2019.12.002.
707 [16] Jeon K.S, Jeong J.I, Pan J.K, Ryu K.W. Effects of the end plates with various shapes and
708 sizes on helical Savonius wind turbines. Renewable Energy 2015;79:167-176.
709 [17] Talukdar P.K, Sardar A, Kulkarni V, Saha U.K. Parametric analysis of model Savonius
710 hydrokinetic turbines through experimental and computational investigations, Energy
711 Conversion and Management 2018;158:36-49. ISSN 0196-8904.
712 https://doi.org/10.1016/j.enconman.2017.12.011.
713 [18] Wenehenubun F, Saputra A, Sutanto H. An experimental study on the performance of
714 Savonius wind turbines related with the number of blades. Energy Procedia 2015;68:297-304.

715 [19] Shamsuddin M.S.M, Kamaruddin N.M. Experimental study on the characterization of the
716 self-starting capability of a single and double-stage Savonius turbin. Results in Engineering
717 2023;17:100854.ISSN 2590-1230.
718 https://doi.org/10.1016/j.rineng.2022.100854.
719 [20] Alom N, Saha U.K. Influence of blade profiles on Savonius rotor performance:
720 Numerical simulation and experimental validation. Energy Conversion and Management
721 2019;186:267-277.
722 [21] Talukdar P.K, Alom N, Rathod U.H, Kulkarni V, Saikia P, Rabha D.K. Wind Tunnel
723 Experiments to Estimate the Performance of a Novel Arc-Elliptical-Bladed Savonius Wind
724 Rotor. In: Mahanta, P., Kalita, P., Paul, A., Banerjee, A. (eds) Advances in Thermofluids and
725 Renewable Energy 2022. Lecture Notes in Mechanical Engineering. Springer, Singapore.
726 https://doi.org/10.1007/978-981-16-3497-0_16.
727 [22] Meri Al Absi S, Hasn Jabbar A, Oudah Mezan S, Ahmed Al-Rawi B, Al_Attabi S.T. An
728 experimental test of the performance enhancement of a Savonius turbine by modifying the
729 inner surface of a blade. Materials Today: Proceedings Part 5 2021;42: 2233-22402021.ISSN
730 2214-7853.
731 https://doi.org/10.1016/j.matpr.2020.12.309.
732 [23] Asadi M, Hassanzadeh R. On the application of semicircular and Bach-type blades in the
733 internal Savonius rotor of a hybrid wind turbine system. Journal of Wind Engineering and
734 Industrial Aerodynamics 2022;221:104903.ISSN 0167-6105.
735 https://doi.org/10.1016/j.jweia.2022.104903.
736 [24] Jia R, Xia H, Zhang S, Weiguang Su, Shuhui Xu. Optimal design of Savonius wind
737 turbine blade based on support vector regression surrogate model and modified flower
738 pollination algorithm. Energy Conversion and Management 2022;270:116247. ISSN 0196-
739 8904.

740 https://doi.org/10.1016/j.enconman.2022.116247.
741 [25] Abdelaziz K.R, Nawar M.A.A, Ramadan A, Attai Y.A, Mohamed, M.H. Performance
742 assessment of a modified of Savonius rotor: Impact of sine and conical blade profiles. Energy
743 2023; 272:127172.ISSN 0360-5442.
744 https://doi.org/10.1016/j.energy.2023.127172.
745 [26] AbdelghafarI, Kerikous E, Hoerner S, Thévenin D. Evolutionary optimization of a
746 Savonius rotor with sandeel-inspired blades. Ocean Engineering 2023; 279:114504.ISSN
747 0029-8018.
748 https://doi.org/10.1016/j.oceaneng.2023.114504.
749 [27] Lee J.H, Lee Y.T, Lim H.C. Effect of twist angle on the performance of Savonius wind
750 turbine. Renewable Energy 2016;89:231-244.
751 [28] Saad A.S, El-Sharkawy I.I, Ookawara S, Ahmed M. Performance enhancement of
752 twisted-bladed Savonius vertical axis wind turbines. Energy Conversion and Management
753 2020;209.112673. ISSN 0196-8904.
754 https://doi.org/10.1016/j.enconman.2020.112673.
755 [29] El-Askary W.A, Saad A.S, AbdelSalam A.M, Sakr I.M. Investigating the performance of
756 a twisted modified Savonius rotor. Journal of Wind Engineering and Industrial Aerodynamics
757 2018;182:344-355.ISSN 0167-6105.
758 https://doi.org/10.1016/j.jweia.2018.10.009.
759 [30] Saad A.S, Elwardany A, El-Sharkawy I.I, Ookawara S, Ahmed . Performance evaluation
760 of a novel vertical axis wind turbine using twisted blades in multi-stage Savonius rotors.
761 Energy Conversion and Management 2021;235:114013.ISSN 0196-8904.
762 https://doi.org/10.1016/j.enconman.2021.114013.
763 [31] Driss Z, Wind Tunnels: Uses and Developments, Mechanical Engineering Theory and
764 Applications, 2019. ISBN: 978-1-53615-898-4. Nova Science Publishers, Inc.

765 [32] Kumar A, Saini R.P. Performance analysis of a Savonius hydrokinetic turbine having
766 twisted blades. Renewable Energy 2017;108:502-22.
767 [33] Kumar A, Saini R.P. Performance analysis of a single stage modified Savonius
768 hydrokinetic turbine having twisted blades. Renewable Energy 2017;113:461-78.
769 [34] Coughtrie A.R, Borman D.J, Sleigh P.A. Effects of turbulence modelling on prediction of
770 flow characteristics in a bench-scale anaerobic gas-lift digester. Bioresour Technol
771 2013;138:297-306.
772 [35] Driss Z, Mlayeh O, Driss D, Maaloul M, Abid MS. Numerical simulation and
773 experimental validation of the turbulent flow around a small incurved Savonius wind rotor.
774 Energy 2014;74:506-17.
775 [36] Mosbahi M, Ayadi A, Chouaibi Y, Driss Z, Tucciarellid T. Performance study of a
776 Helical Savonius hydrokinetic turbine with a new deflector system design. Energy Conversion
777 and Management 2019;194:55-74.
778 [37] Jaohindy P, McTavish S, Garde F, Bastide A. An analysis of the transient forces acting
779 on Savonius rotors with different aspect ratios. Renewable Energy2013;55:286-95.
780 [38] Sharma S, Sharma R.K. Performance improvement of Savonius rotor using multiple
781 quarter blades–A CFD investigation. Energy Conversion and Management 2016;127:43-54.
782 [39] Roy S, Ducoin A. Unsteady analysis on the instantaneous forces and moment arms acting
783 on a novel Savonius-style wind turbine. Energy Conversion and Management 2016;121:281-
784 296.
785 [40] Nasef M.H, El-Askary W.A, AbdEL-Hamid A.A, Gad H.E. Evaluation of Savonius
786 rotor performance: Static and dynamic studies. Journal of Wind Engineering and Industrial
787 Aerodynamics 2013;123:1-11

788 [41] Damak A, Driss Z, Abid M.S. Optimization of the helical Savonius rotor through wind
789 tunnel experiments, Journal of Wind Engineering and Industrial Aerodynamics 2018; 174:80-
790 93.ISSN 0167-6105
791 https://doi.org/10.1016/j.jweia.2017.12.022.
792 [42] Zadeh MN, Pourfallah M, Sabet SS. et al. Performance assessment and optimization of a
793 helical Savonius wind turbine by modifying the Bach's section. SN Appl. Sci. 2021;**3**:739.
794 https://doi.org/10.1007/s42452-021-04731-0
795 [43] Kamoji M.A, Kedare S.B, Prabhu S.V. Performance Tests on Helical Savonius Rotor.
796 Renewable Energy 2009;34:521-529.
797 [44] Anbarsooz M. Aerodynamic performance of helical Savonius wind rotors with 30° and
798 45° twist angles: Experimental and numerical studies. J Power and Energy 2016;0:1-12.

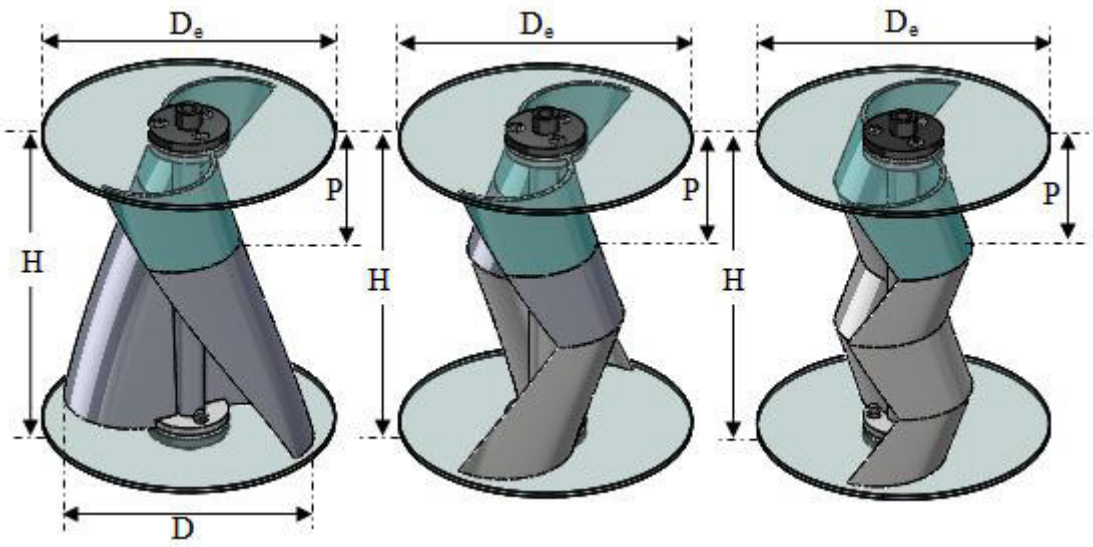

Helical rotor Delta bladed rotor Two-stage delta bladed rotor

(a) Digital models

(b) 3D printed rotors

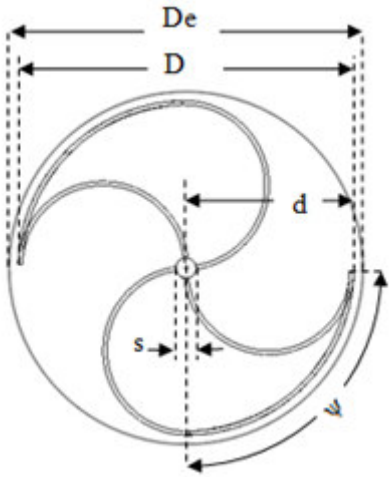

(c) Geometrical parameters

Figure 1. The rotor blade shapes covered in the current study.

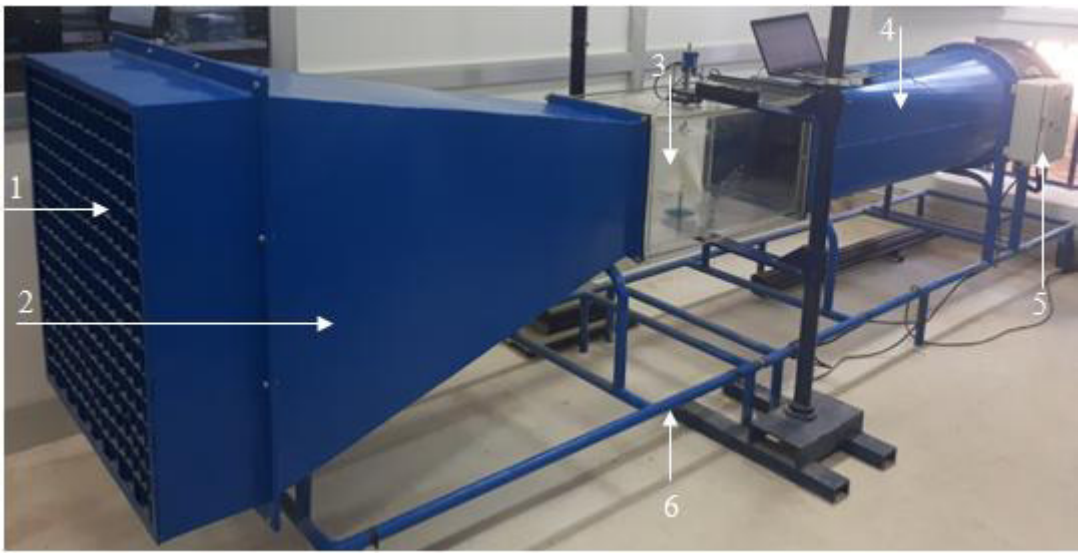

1 Settling chamber
2 Diffuser
3 Test section
4 Collector
5 Drive section
6 Structure

Figure 2. Wind tunnel test facility.

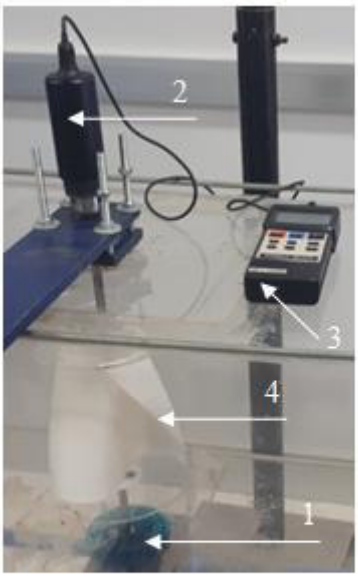

1 Gradual disc
2 Static torque meter sensor
3 Digital display
4 Rotor

Figure 3. Static measurement apparatus.

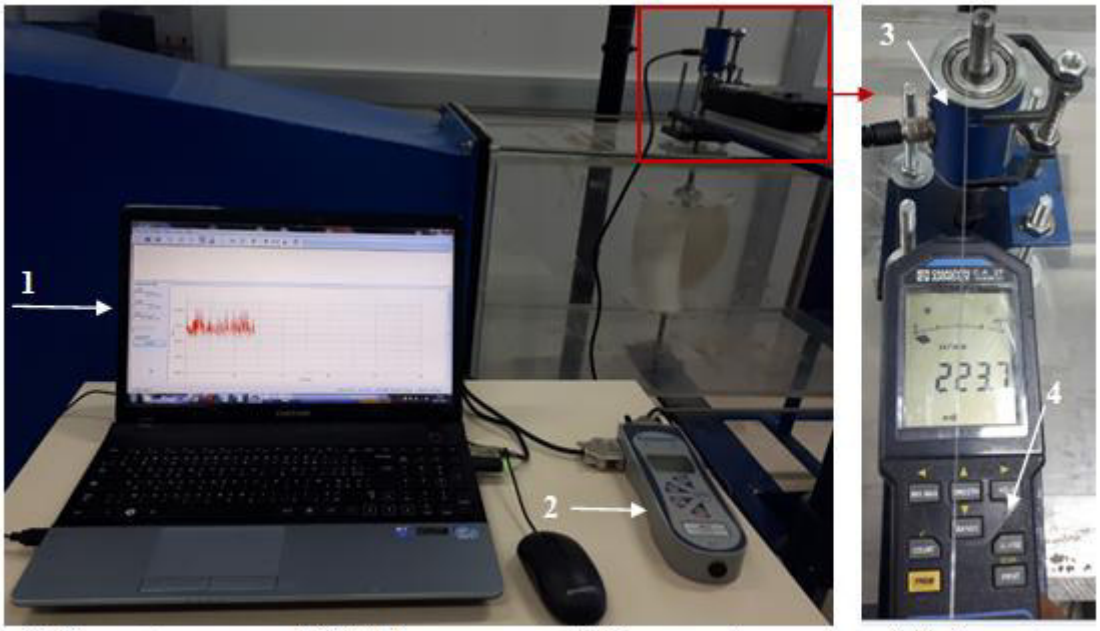

1 Computer acquisition | 2 Digital display | 3 Torque meter sensor | 4 Tachometer

Figure 4. Dynamic measurement apparatus.

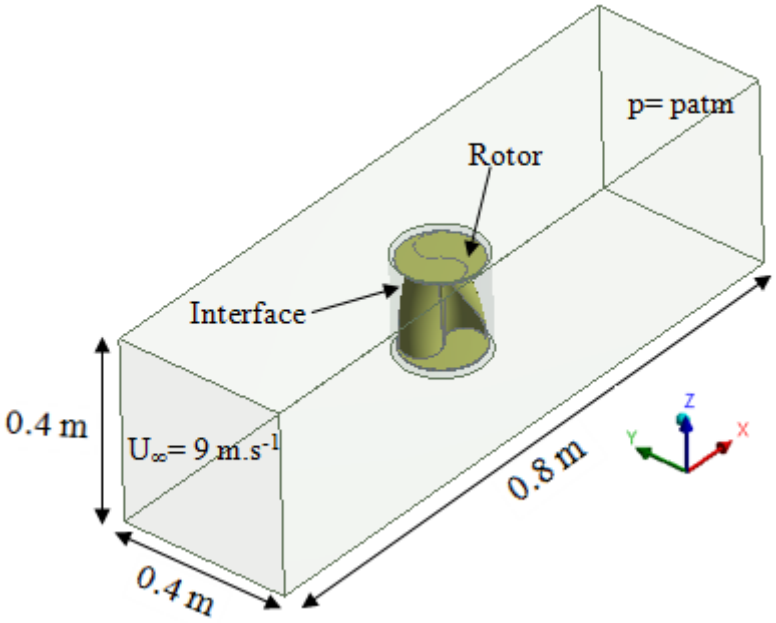

Figure 5. Overall domain and boundary condition details.

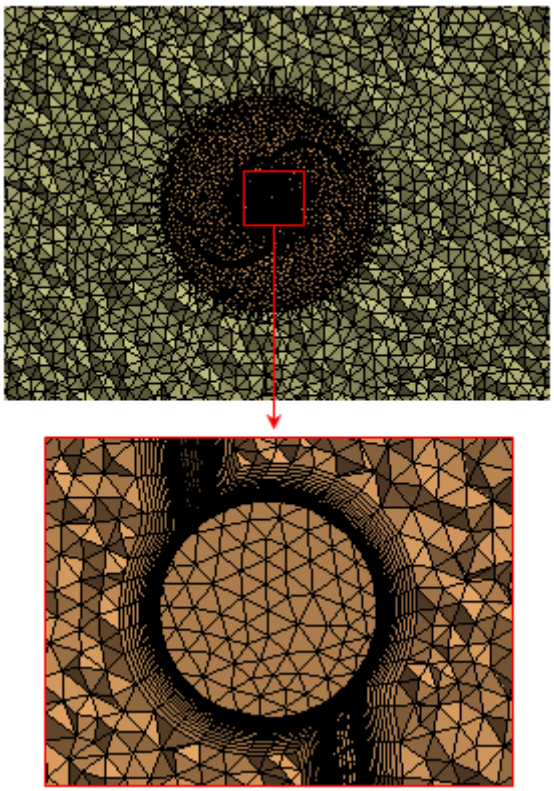

Figure 6. Grid generation.

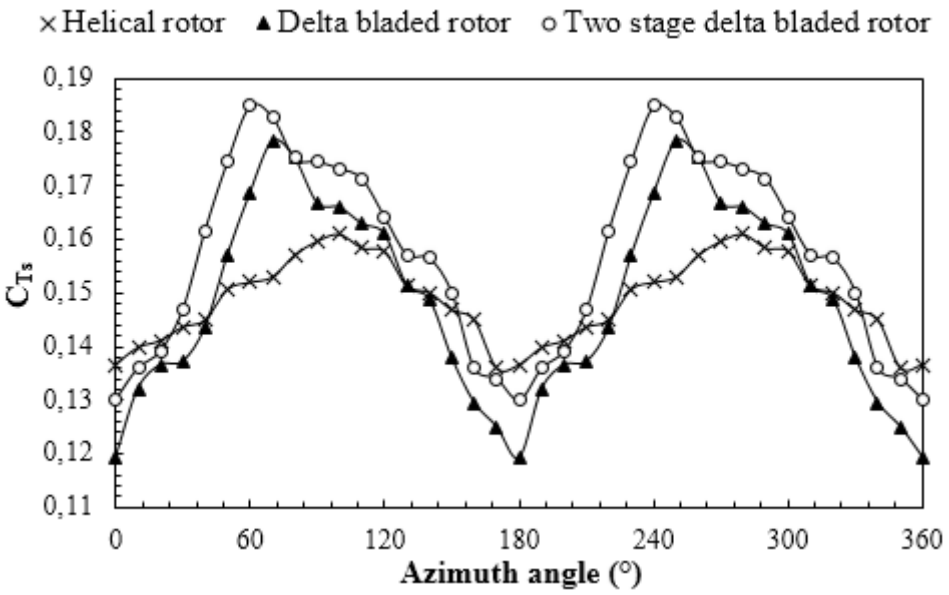

Figure 7. Static torque coefficient versus azimuth angle.

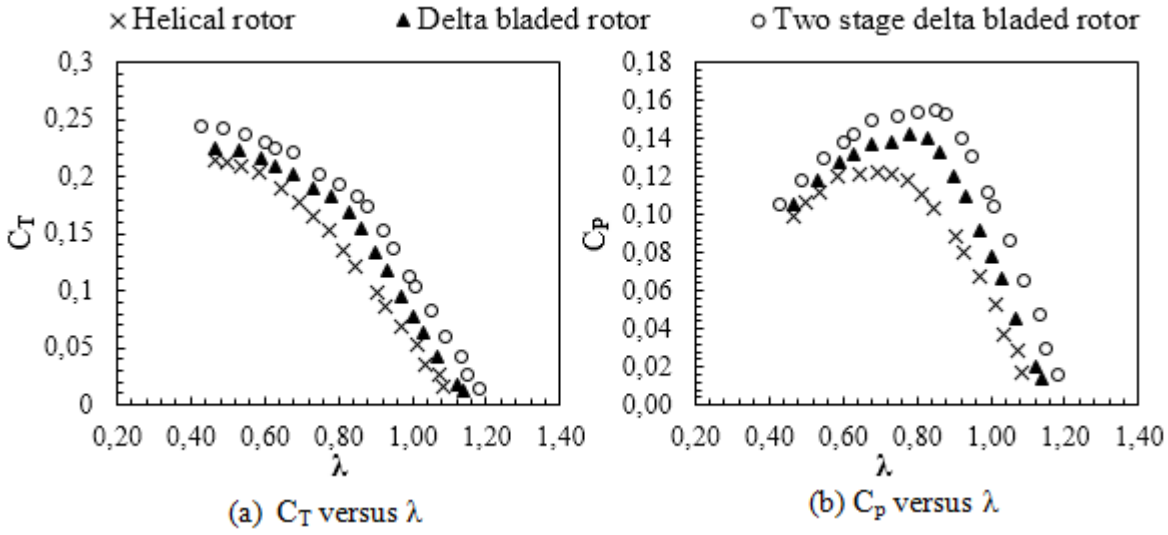

Figure 8. Performance characteristics.

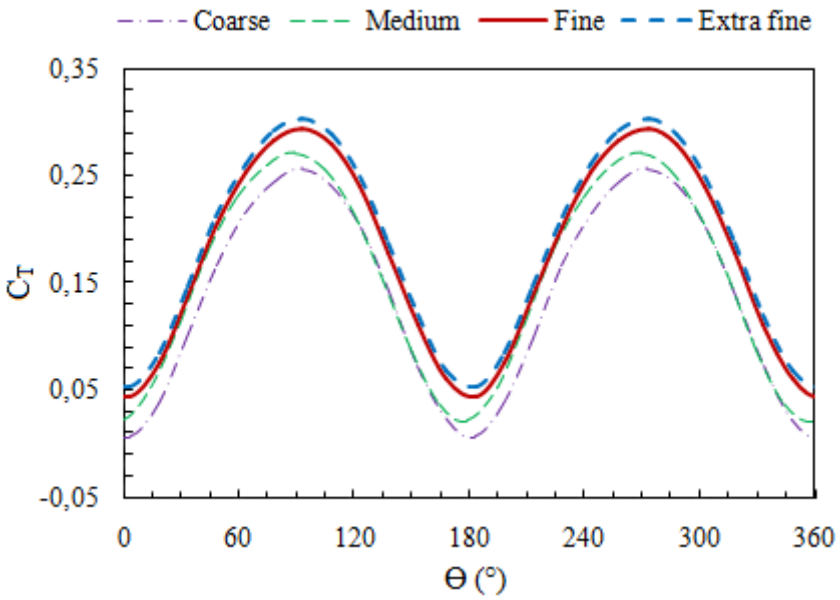

Figure 9. Grid form test.

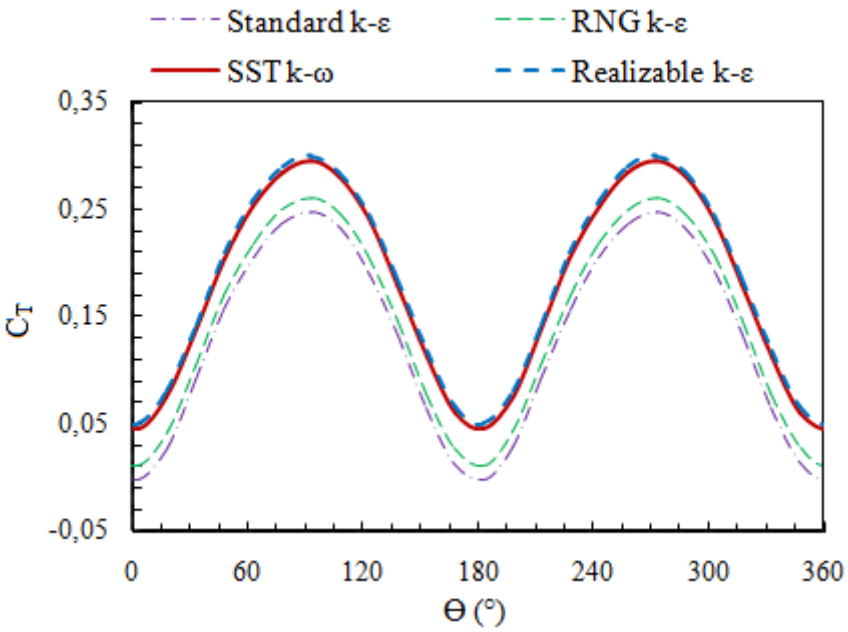

Figure 10. Turbulence model test.

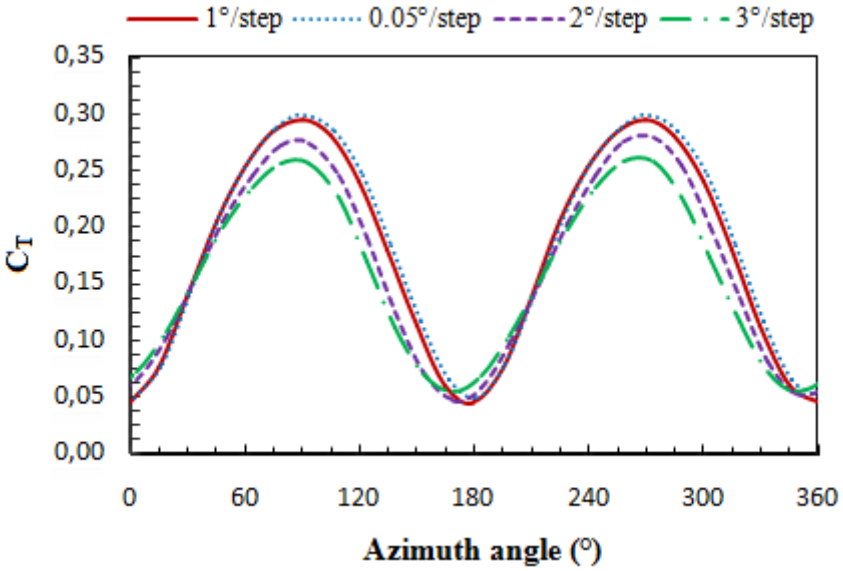

Figure 11. Time step independency test.

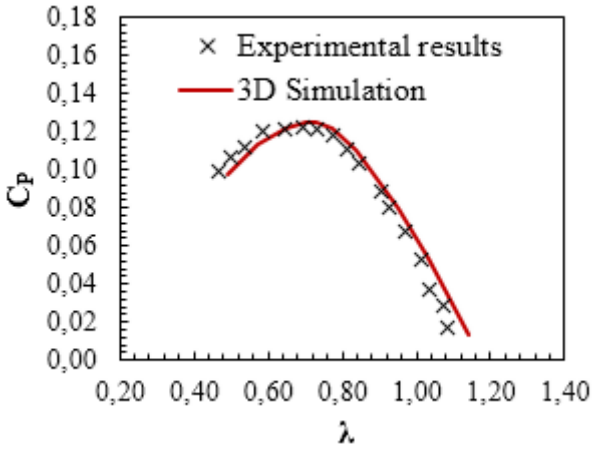

Figure 12. Numerical model validation.

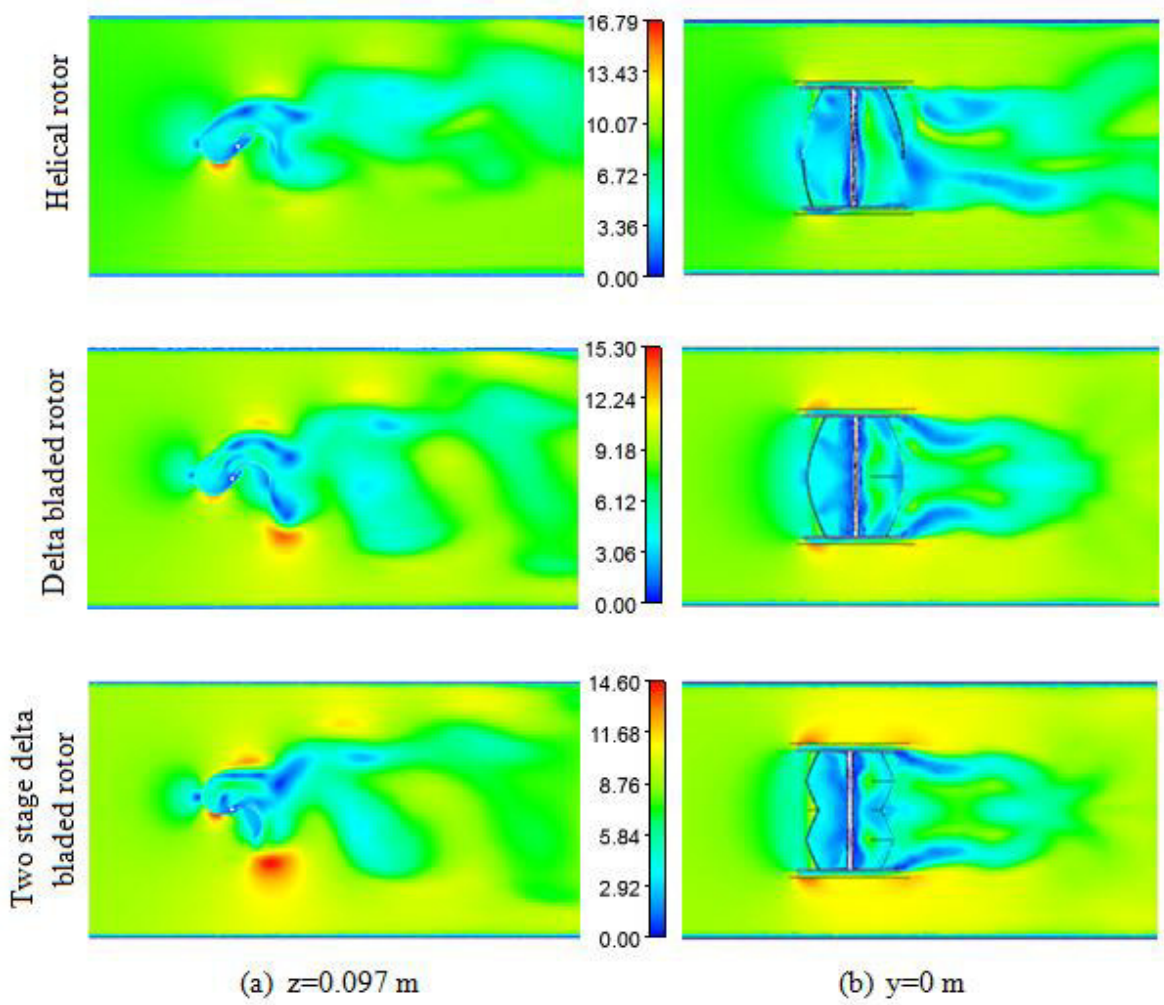

Figure 13. Magnitude velocity ($m.s^{-1}$) distribution.

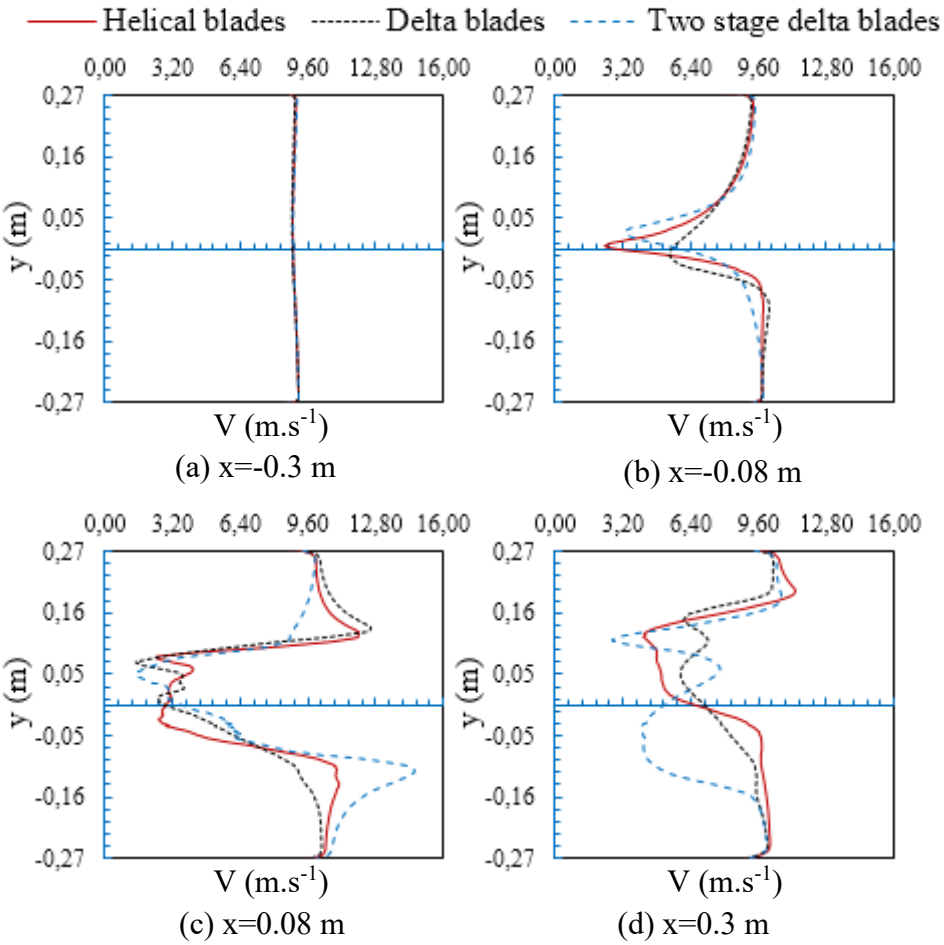

Figure 14. Velocity ($m.s^{-1}$) profiles.

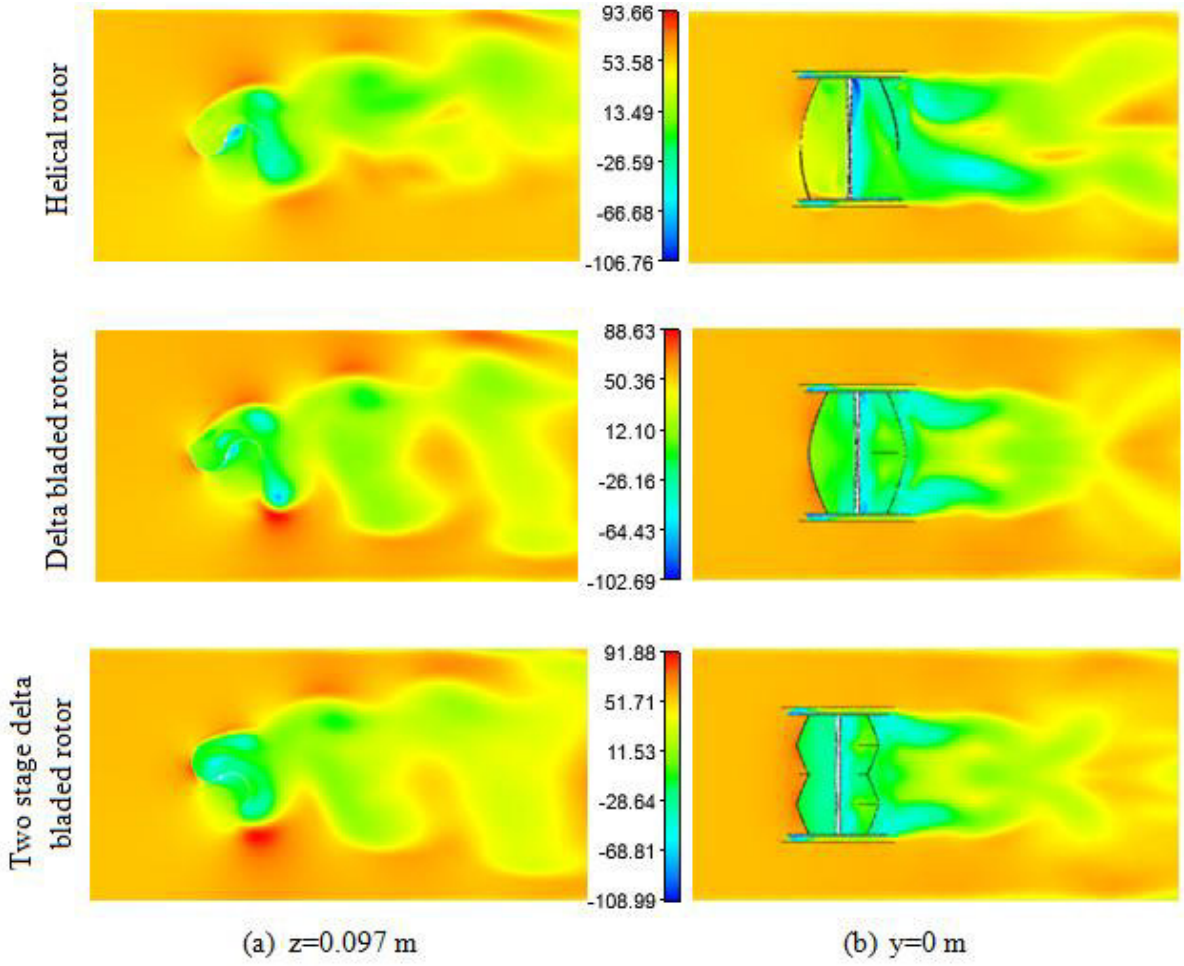

Figure 15. Total pressure (Pa) distribution.

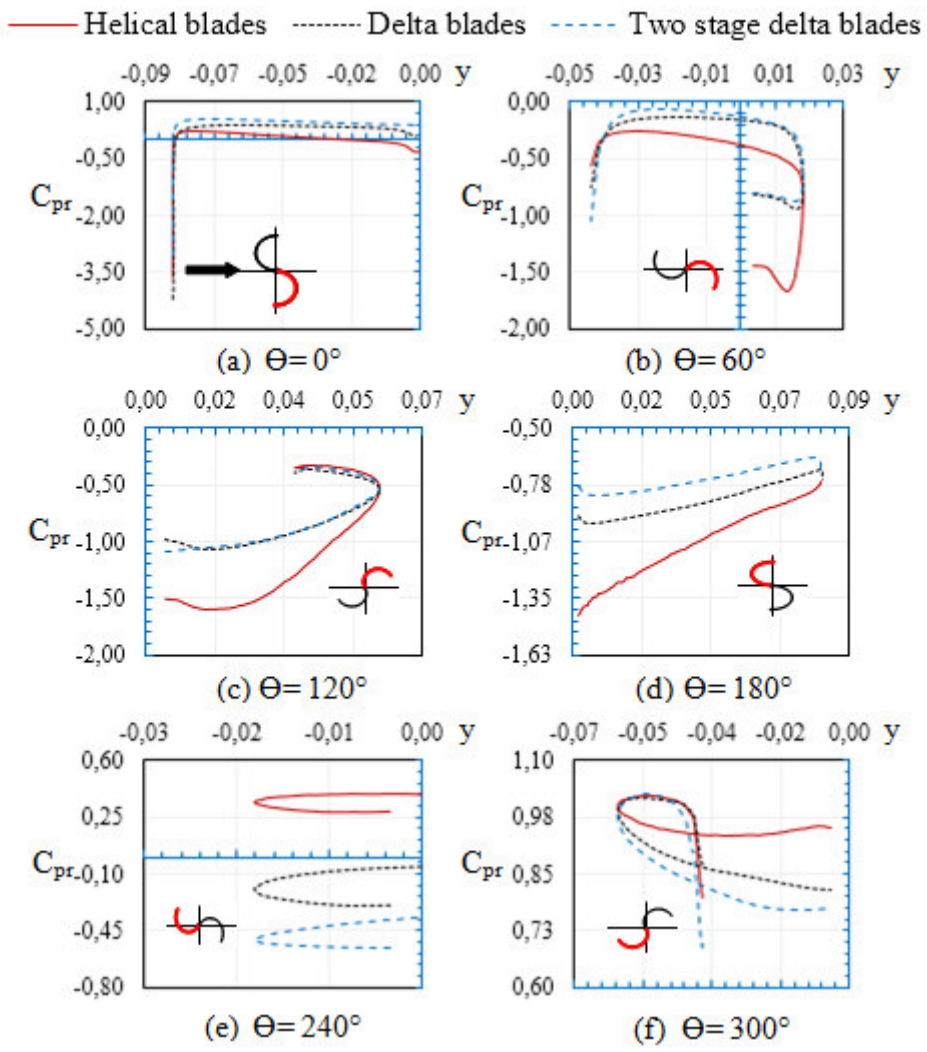

Figure 16. Pressure coefficient on the concave side of the advancing blade during one revolution.

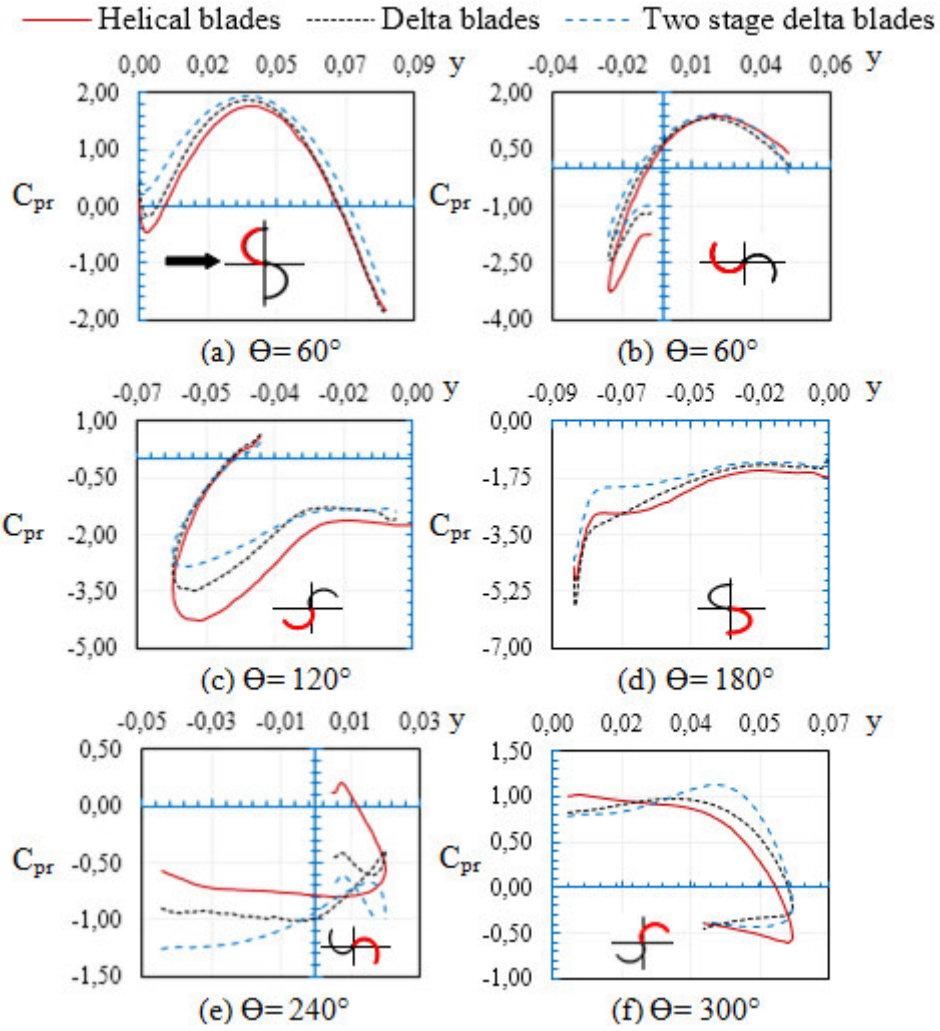

Figure 17. Pressure coefficient on the convex side of the returning blade during one revolution.

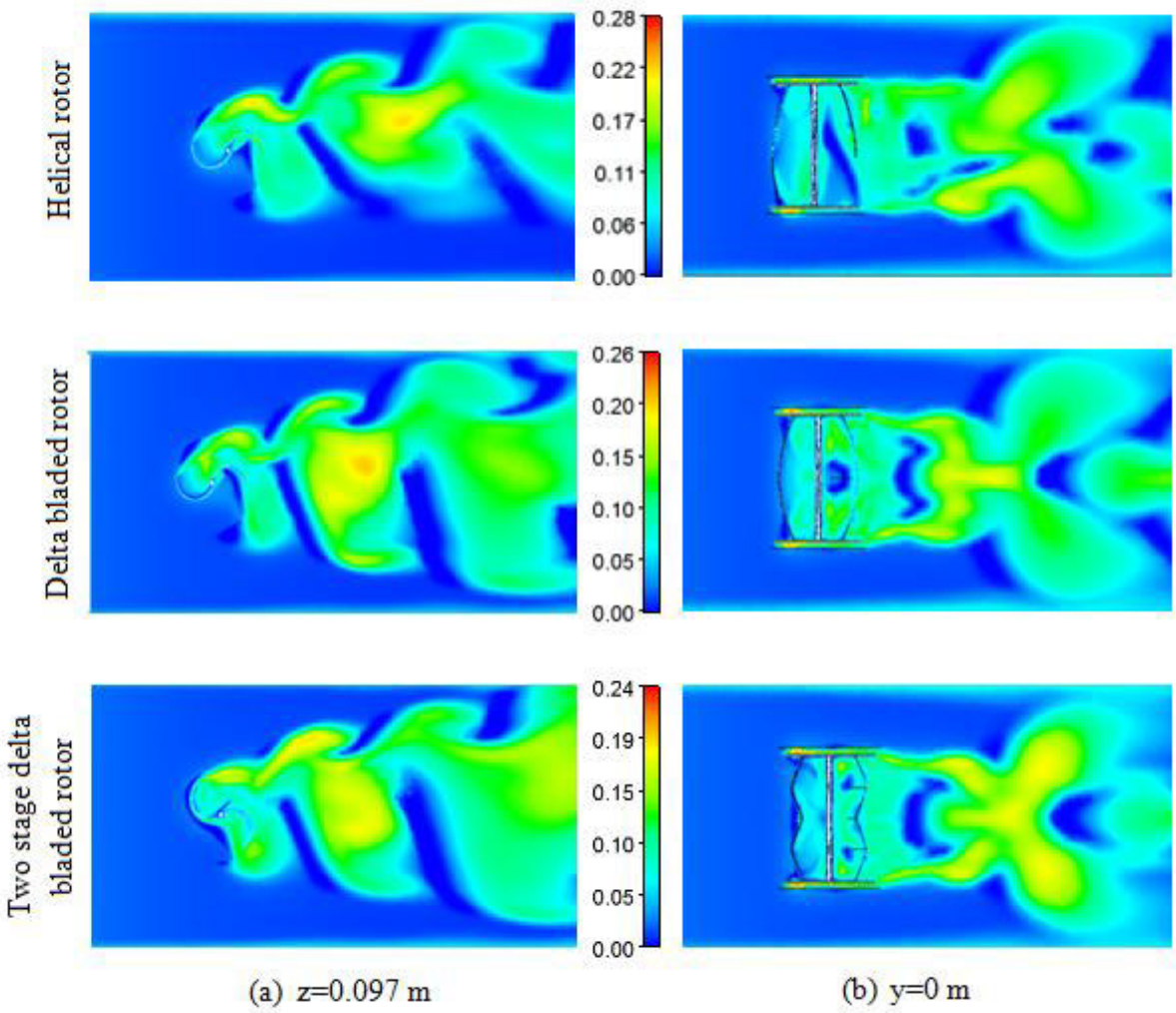

Figure 18. Turbulent intensity distribution.

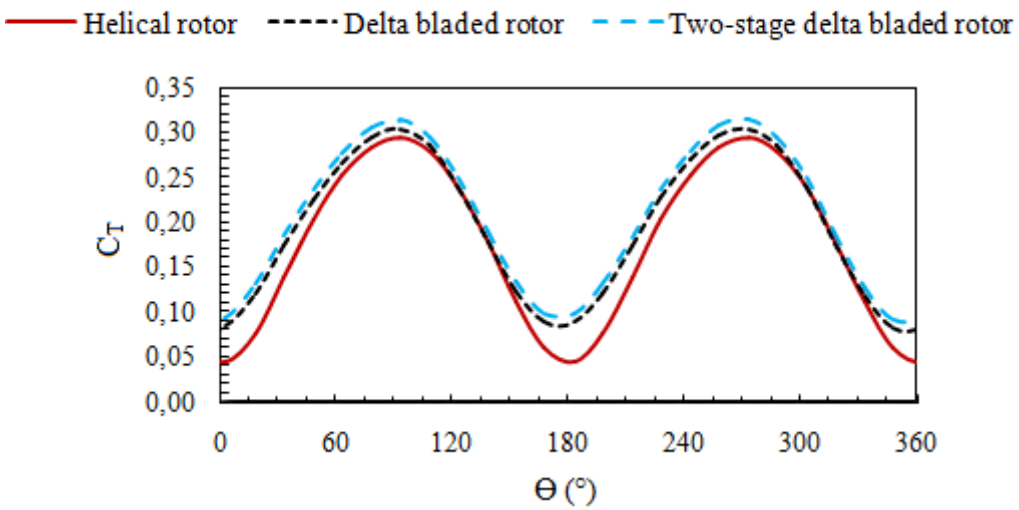

Figure 19. Torque coefficient at λ= 0.73 for the different rotor blade shapes.

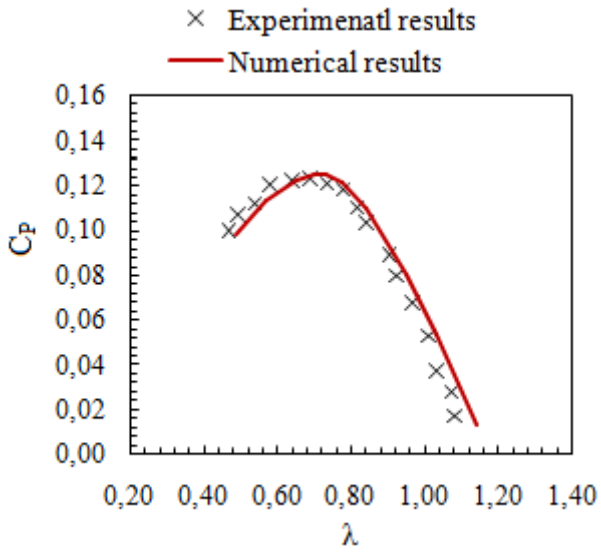

(a) Helical rotor

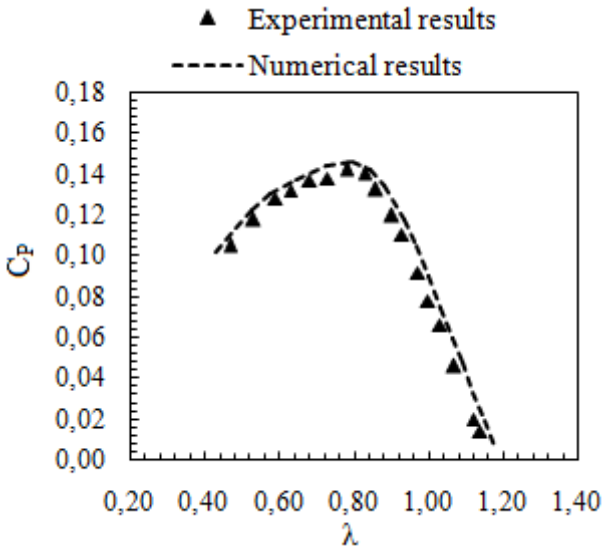

(b) Delta bladed rotor

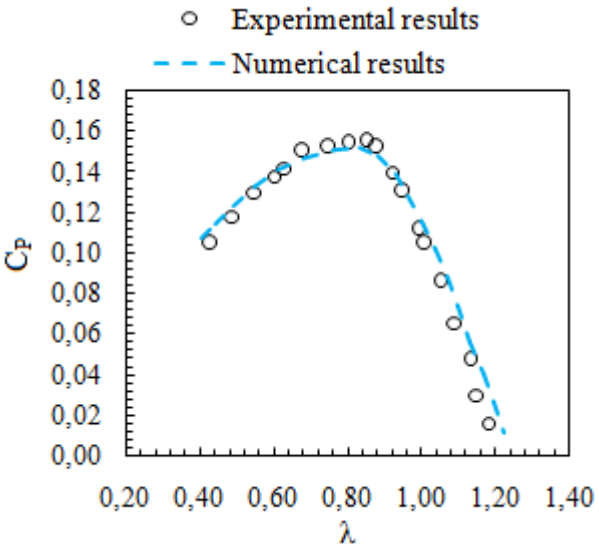

(c) Two-stage delta bladed rotor

Figure 20. Comparison between experimental and numerical results for different rotor blade shapes.

Table 1. Geometrical parameters of the studied helical Savonius rotors.

		Geometrical parameters						
Savonius rotors	Blade profile	S (mm)	H (mm)	D (mm)	D_e (mm)	e (mm)	d (mm)	Ψ (°)
Helical	Semi-circular	10	200	160	165	0	80	90
Delta bladed	Semi-circular	10	200	160	165	0	80	90
Two-stage delta bladed	Semi-circular	10	200	160	165	0	80	90

Table 2. Ananometer specifications.

Description	Type AM 4204
Manufacturer	Lutron
Probe type	Thermal
Measurement range	0.2 up to 20 $m.s^{-1}$
Precision	±0.1 %
Resolution	0.1 $m.s^{-1}$

Table 3. Static digital torque meter specifications.

Description	Type TQ 8800
Manufacturer	Lutron
Measurement range	0 up to147.1 N.Cm
Precision	±1.5%
Resolution	0.1 N.Cm
Dimensions	180*72*32 mm

Table 4. Tachometer specifications.

Description	Type CA-1727
Measurement range	6 up to 10000 RPM
Precision	10^{-4}
Resolution	0.0006 RPM
Stability	±6 points
Autonomy	250 measurements in 5 min
Dimension	216*72*47 mm

Table 5. Dynamic digital torque meter specifications.

Description	Type AFTI
Manufacturer	Mecmesin
Measurements range	0-2 up to 150 N.m
Precision	±1%
Dimensions	32*70*201mm

Table 6. Experimental uncertainties on λ, C_{Ts}, C_p and C_T

Parameter	Uncertainty		
	Helical rotor	Delta bladed rotor	Two-stage Delta bladed rotor
λ	2.8 %	2.5 %	2.1 %
C_{Ts}	4.1 %	3.8 %	3.5 %
C_T	2.2%	2.5 %	2.3 %
C_p	2.9%	2.7 %	2.8 %

Table 7. Experimental error for the used measurement instruments.

Measurement instrument	Experimental error
Anemometer	1 %
Tachometer	3.6 %
Static torque meter	4 %
Dynamic torque meter	2.8 %

Table 8. Comparison with previous studies.

Reference	Methodology	Blade profile	Twist angle (°)	$C_{p\ max}$	λ at $C_{p\ max}$	Wind speed ($m.s^{-1}$)	A_r	O_r
Lee et al.[27]	Numerical and experimental	Semi-circular	45	0.13	0.54	10	1.3	0
Saad et al.[28]	Numerical	Semi-circular	45	0.232	0.8	10	1	0
Damak et al.[41]	Numerical and Experimental	Bach	90	0.2	0.75	12	0.7	0
Zadeh et al.[42]	Numerical and experimental	Bach developed	135	0.14	0.6	10	2	0
Kamoji et al. [43]	Experimental	Semi-circular	90	0.175	0.9	14	0.88	0
Anbarsooz et al.[44]	Numerical and experimental	Semi-circular	45	0.115	0.7	9	1	0
Current study	Numerical and experimental	Semi-circular	90	0.124	0.73	9	0.825	0
		Delta-bladed	90	0.148	0.8	9	0.825	0
		Two stage delta-bladed	90	0.152	0.88	9	0.825	0

Highlights

1- Savonius wind turbines suffers low power efficiency.

2- This research paper proposes novel blade shapes of the helical Savonius rotor.

3- In this study, three rotors have been investigated numerically and experimentally.

4- The blade shape affects the performance of the helical Savonius rotor.

5- The maximum power coefficient was increased by 29.5% over the helical Savonius rotor.